Mon. Not. R. Astron. Soc. **358,** 233–255 (2005) doi:10.1111/j.1365-2966.2005.08779.x

On the evolutionary status of early-type galaxies in clusters at $z \approx 0.2$ – I. The Fundamental Plane

Alexander Fritz,[1⋆] Bodo L. Ziegler,[1] Richard G. Bower,[2] Ian Smail[2] and Roger L. Davies[3]

[1] *Universitäts–Sternwarte Göttingen, Geismarlandstraße 11, D-37083 Göttingen, Germany*
[2] *Institute for Computational Cosmology, University of Durham, South Road, Durham DH1 3LE*
[3] *University of Oxford, Astrophysics, Denys Wilkinson Building, Keble Road, Oxford OX1 3RH*

Accepted 2005 January 4. Received 2004 December 20; in original form 2004 October 7

ABSTRACT

We investigate a spectroscopic sample of 48 early-type galaxies in the rich cluster Abell 2390 at $z = 0.23$ and 48 early-type galaxies from a previously published survey of Abell 2218 at $z = 0.18$. The spectroscopic data of A 2390 are based on multi-object spectroscopy using the multi-object spectrograph for Calar Alto at the 3.5-m telescope on Calar Alto Observatory and are complemented by ground-based imaging using the 5.1-m Hale telescope and *Hubble Space Telescope* (*HST*) observations in the F555W and F814W filters. Our investigation spans a broad range in luminosity ($-20.5 \geqslant M_r \geqslant -23.0$) and a rather wide field of view of $1.53\,h_{70}^{-1} \times 1.53\,h_{70}^{-1}$ Mpc^2.

As the A 2218 and A2390 samples are very similar, we can combine them and analyse a total number of 96 early-type (E+S0) galaxies at $z \sim 0.2$. Using the ground-based data only, we construct the Faber–Jackson relation (FJR) for all 96 E+S0 galaxies and detect a modest luminosity evolution with respect to the local reference. The average offset from the local FJR in the Gunn r band is $\Delta\,\overline{M}_r = 0.32 \pm 0.22$ mag. Similar results are derived for each cluster separately. Less massive galaxies show a trend for a larger evolution than more massive galaxies. *HST*/WFPC2 surface brightness profile fits were used to derive the structural parameters for a subsample of 34 E+S0 galaxies. We explore the evolution of the Fundamental Plane (FP) in Gunn r, its projections on to the Kormendy relation and the M/L ratios as a function of velocity dispersion. The FP for the cluster galaxies is offset from the local Coma cluster FP. At a fixed effective radius and velocity dispersion our galaxies are brighter than their local counterparts. For the total sample of 34 E+S0 cluster galaxies which enter the FP we deduce only a mild evolution with a zero-point offset of 0.10 ± 0.06, corresponding to a brightening of 0.31 ± 0.18 mag. Elliptical and lenticular galaxies are uniformly distributed along the FP with a similar scatter of 0.1 dex. Within our sample we find little evidence for differences between the populations of elliptical and S0 galaxies. There is a slight trend that lenticulars induce on average a larger evolution of 0.44 ± 0.18 mag than ellipticals with 0.02 ± 0.21 mag. The M/L ratios of our distant cluster galaxies at $z = 0.2$ are offset by $\Delta\log(M/L_r) = -0.12 \pm 0.06$ dex compared with those of Coma. Our results can be reconciled with a passive evolution of the stellar populations and a high formation redshift for the bulk of the stars in early-type galaxies. However, our findings are also consistent with the hierarchical formation picture for rich clusters, if ellipticals in clusters had their last major merger at high redshift.

Key words: galaxies: clusters: individual: Abell 2218 – galaxies: clusters: individual: Abell 2390 – galaxies: elliptical and lenticular, cD – galaxies: evolution – galaxies: fundamental parameters – galaxies: kinematics and dynamics.

⋆E-mail: afritz@uni-sw.gwdg.de

1 INTRODUCTION

Since the first development and application of theoretical galaxy models (e.g. Larson 1975; Toomre 1977) much progress has been achieved to explore the evolution of early-type (E+S0) galaxies. Nevertheless, one of the key questions of early-type galaxy formation and evolution has not been fully answered as yet: when and within what time-scales have the stellar populations of early-type galaxies been formed?

In the hierarchical galaxy formation picture the formation histories of early-type galaxies in cluster and low-density environments are significantly different (Baugh, Cole & Frenk 1996; Kauffmann & Charlot 1998). Merging of galaxies and the infall of new cold gas from the galaxy haloes are the main drivers of structure evolution. Clusters are formed out of the highest peaks of primordial density fluctuations and most stars of massive cluster ellipticals are generated at high redshift ($z \geqslant 2$), which is in agreement with observational findings (e.g. Ziegler & Bender 1997; van Dokkum et al. 1998). However, explicit age variations between early-type cluster galaxies and E+S0 galaxies in low-density regions are predicted. For clusters, models predict ellipticals to have a mean luminosity-weighted age of 9.6 Gyr and lenticular galaxies to be younger by $\sim$1 Gyr (Baugh et al. 1996; Cole et al. 2000). Both types indicate a weak trend of fainter galaxies being older. In contrast, for early-type galaxies in low-density regions the hierarchical cluster models predict a broader age spread over a larger luminosity range and mean luminosity-weighted ages of $\sim$5.5 Gyr.

Numerous observational studies imply four main types of evidence for a high-redshift formation of early-type galaxies: (i) the homogenous stellar populations of E+S0 galaxies seen in tight correlations between colours/absorption line strengths and velocity dispersion and in the Fundamental Plane (FP), which combines kinematics with structural properties; (ii) the [Mg/Fe] overabundance; and (iii) the weak evolution in colours and line strengths with redshift.

In the nearby Universe, inconsistent results have been acquired regarding any possible difference between field and cluster galaxies. For example, de Carvalho & Djorgovski (1992) derived from a subset of cluster and field early-type galaxies taken from the 'Seven Samurai' group (Djorgovski & Davis 1987; Faber et al. 1989) that field ellipticals show a larger scatter in their properties indicating that they consist of younger stellar populations than cluster galaxies. James & Mobasher (1999) investigated near-infrared (NIR) spectra of 50 ellipticals in three nearby clusters and in the field, using the CO (2.3-μm) absorption feature to explore the presence of an intermediate-age population. They detected no stronger CO absorption for the field ellipticals. Very isolated field ellipticals show a very homogenous population and a small range of metallicity with no sign of recent star formation (SF). In groups, ellipticals have a wide range in metallicity, mostly showing evidence for an intermediate-age population, whereas in rich clusters they exhibit intermediate properties in metallicity and CO absorption. Bernardi et al. (1998) analysed a large sample of ENEAR field and cluster galaxies and found slight zero-point changes in the Mg_2–σ relation. They explain this as an age difference, with field objects being younger by $\sim$1 Gyr. However, they conclude that the bulk of stellar populations of E+S0 in both environments has been formed at high redshifts ($z \gtrsim 3$). Kuntschner et al. (2002) detected, in a sample of nine local early-type galaxies (five morphologically disturbed) in low-density environments (LDR), no strong ongoing SF. The results were compared with cluster E+S0s in Fornax. The ages of the LDR galaxies are spread over a broad distribution, similar to that of Fornax S0 galaxies, being on average younger by 2–3 Gyr than the E+S0s in Fornax. These LDR galaxies indicate 0.2 dex *higher* metallicities (in conflict with semi-analytical models) than their cluster representatives, which suggests that the formation of E+S0 galaxies at low densities continues to $z \lesssim 1$, whereas in clusters most stars have already been generated at $z \gtrsim 2$. Recently, Sánchez-Blázquez et al. (2003) studied 98 E+S0 galaxies in the field and in clusters and found higher C4668 and CN_2 absorption-line strengths for the field population. They interpret this as a difference in abundance ratios arising from different star formation histories. However, both field and cluster E+S0s show similar relations in Mg_b–σ and $\langle$Fe$\rangle$–σ.

At higher redshift differences between field and cluster galaxies should become more apparent. Recent results from investigations based on the FP at intermediate redshift ($z \leqslant 0.5$), indicate no significant variations between the cluster and field early-type populations (Treu et al. 2001b; van Dokkum et al. 2001; Rusin et al. 2003). With respect to the mean age of these populations, field galaxies seem to comprise slightly younger stars than the cluster population, whereas the majority of stars must have formed at a much higher redshift of $z_f > 2$. However, at higher redshift ($z \sim 0.7$), some studies derive a significant offset between field and cluster galaxies (Treu et al. 2002).

In recent years a multiplicity of investigations of distant rich clusters have been performed (Dressler et al. 1997; Ellis et al. 1997; van Dokkum et al. 1998; Stanford, Eisenhardt & Dickinson 1998; Kelson et al. 2000b; van Dokkum et al. 2000; Ziegler et al. 2001; Treu et al. 2003; Wuyts et al. 2004). Most of these studies can be reconciled with the picture of a monolithic collapse with a high-redshift formation of the stellar populations of E+S0 galaxies. Results from these distant clusters have not found any differences in the properties of E+S0 galaxies (e.g. Kelson et al. 2000b). Recently, in a re-analysis of two high-redshift clusters at $z = 0.58$ and 0.83 no environmental dependence of the FP residuals was detected (Wuyts et al. 2004). When looking at the residuals of the FP, and suggesting that the residuals correlate with environment, it is difficult to distinguish whether this effect is due to changes in velocity dispersion, size or luminosity of the galaxies. Selection effects have a strong influence on the parameters and can also mimic possible correlations. In a study on $\sim$9000 early-type galaxies from the SDSS (Bernardi et al. 2003), a weak correlation between the local density and the residuals from the FP was revealed, in the sense that the residuals in the direction of the effective radii increase slightly as the local density increases. However, the offset is quite small and subject to selection and evolutionary effects. The open question still to address is, how this dependence occurs.

Looking at the morphology, the formation and evolution of lenticular galaxies is different and stands in contrast to elliptical galaxies. Deep studies of galaxies in distant rich clusters using the *WFPC2* camera onboard the *Hubble Space Telescope* (*HST*) revealed that S0 galaxies show a rigorous evolution with redshift in these dense environments (e.g. Dressler et al. 1997). Although S0 galaxies form the dominant population in local rich clusters of $\sim$60 per cent, at intermediate redshift ($z \sim 0.5$) spiral and disturbed galaxies comprise the major part of the luminous galaxies, whereas S0 galaxies are less abundant (10–20 per cent). Schade et al. (1999) studied early-type field galaxies at intermediate redshifts ($z \sim 0.5$) and detected [O II] λ3727 emission lines in approximately one-third of these galaxies, which indicates ongoing star formation. Furthermore, in approximately the same fraction of faint spheroidal HDF galaxies significant variations of internal colours were found, frequently showing objects with blue cores (Menanteau, Abraham & Ellis 2001). The authors conclude that at $z \sim 1$ approximately half of the field S0

galaxies show clear signs of star formation activity. Using deep optical and NIR imaging, Smail et al. (2001) revealed differences between more luminous ($\gtrsim 0.5 L_K^*$) and less luminous ($\lesssim 0.1 L_K^*$) early-type galaxies in A 2218. The faintest S0s show a wide spread in the colours, and ∼30 per cent of these S0s exhibit on average younger ages (2–5 Gyr).

These results seem to imply that galaxy transformation via interaction is an important phenomenon in clusters. As a result of the large velocity dispersion, mergers are less frequent in rich clusters, whereas effects such as ram-pressure stripping by the hot intracluster medium (ICM) or tidal interactions between the galaxies are more likely. A unique mechanism for the transformation into S0 galaxies is still missing to explain the strong decrease in the frequency of S0s over the last 5 Gyr ($z \sim 0.5$). A possible scenario is that field spiral galaxies falling into the cluster centre experience a starburst phase, resulting in the Butcher–Oemler effect. Ram-pressure stripping by the ICM (also possibly through tidal stripping) over a short time-scale of less than 1 Gyr, could cause the widespread and rapid decline in star formation leading to post-starburst galaxies and red passive spiral galaxies (e.g. Barnes & Hernquist 1992). Harassment by the tidal field of the galaxy cluster and high-speed encounters have a non-negligible effect on the subsequent passive evolution of a galaxy by removing stars from the disc which may end up in an S0 galaxy (Moore et al. 1996; Poggianti et al. 1999).

In terms of structural parameters, elliptical galaxies comprise not a single homogenous group of galaxies but encompass two different groups, *disky* and *boxy* ellipticals (Bender 1988; Bender, Döbereiner & Möllenhoff 1988; Kormendy & Bender 1996). The shape of these galaxies is very important as it correlates with other physical properties, such as luminosity, shape, rotation (axis) and core profile. Recently, the origin of disky and boxy ellipticals was investigated (Naab, Burkert & Hernquist 1999; Naab & Burkert 2003). Equal-mass mergers result in an anisotropic system with slow major axis rotation and a large amount of minor-axis rotation (boxy elliptical), whereas unequal-mass merger of mass ratios of 3:1 and 4:1 lead to a rotationally supported system with only a small rotation along the minor-axis (disky elliptical). In general, giant *high-luminous* ellipticals preferably contain *boxy* isophotes, whereas *low-luminous* ellipticals comprise a *disky* structure. Could they possibly have a different evolution? At intermediate redshifts we cannot distinguish between disky and boxy galaxies. However, with respect to our large sample we are able separate low- from high-luminosity galaxies and look for possible differences in their evolution. The results of such a comparison would give conclusions if the two types of ellipticals were to undergo different formation scenarios.

Cluster environments provide the opportunity to observe a larger number of early-type galaxies with multi-object spectroscopy simultaneously. Furthermore, at a redshift of $z \sim 0.2$, the cluster galaxies are bright enough to observe even sub-L^* systems with 4-m class telescopes, while still representing a lookback time of ∼3 Gyr, which is adequate to address evolutionary questions. To look for the environmental dependence, it is desirable to investigate possible radial dependences on the age and the metallicity of stellar populations with a large sample of early-type galaxies. Therefore, we have undertaken a programme to acquire high-quality spectra of a large number of early-type galaxies in two rich clusters, $N = 48$ for Abell 2218 and $N = 48$ in the case of Abell 2390, across a wide range in luminosity (down to $M_B = M^* + 1$, with $M^* = -19.5 + 5 \log h_{70}$; corresponding to $-19.2 \geqslant M_B \geqslant -24.2$ for $z = 0.23$) and a wide field of view (FOV) (∼10 × 10 arcmin^2). Each cluster centre has been observed with *HST*, therefore allowing accurate structural parameter determinations. As already demonstrated in Ziegler et al. (2001), both clusters may well serve in the future as suitable benchmarks for comparison with rich, high-redshift clusters, as aperture corrections are less crucial than, for example, for the Coma cluster.

The analysis and results of our study of the cluster A 2218 are discussed in detail in Ziegler et al. (2001, hereafter Z01). In this article, we present the investigation of A 2390. Combining these two large data samples, a total number of 34 E+S0 galaxies enter the FP, which represents – apart from the study of Kelson et al. (2000b) – the most extensive investigation on early-type cluster galaxies at intermediate redshift. Our study is dedicated to exploring intrinsically low-luminosity elliptical and S0 galaxies at redshifts where some evolution is visible and over a wide FOV in order to look for environmental variations of the evolution of E+S0 galaxies. Another important aim of this work is also to break the 'age–metallicity' degeneracy of early-type galaxies. In a forthcoming paper we will explore the evolution of the A 2390 stellar populations in age, metallicity and abundance ratios by analysing absorption-line strengths (e.g. Hβ, Mg$_b$, Fe-indices), and comparing them with stellar population models.

The paper is organized as follows. The photometry on the ground-based images of A 2390 and the *HST* structural analysis are presented in Section 2. Spectroscopic observations of the cluster A 2390, the sample selection and reduction of the spectra are described in Section 3. In Section 4 the evolutionary status of the rich clusters A 2390 and 2218 at $z \sim 0.2$ is illustrated. Results for both clusters derived with scaling relations such as the Faber–Jackson relation, FP and the evolution of the M/L ratio are given in Section 5. A summary of our results is presented in Section 6.

In this paper we assume the concordance cosmology for a flat Universe with $\Omega_m = 0.3$, $\Omega_\Lambda = 0.7$ and $H_0 = 70$ km s^{-1} Mpc^{-1}. This results for the nearby Coma comparison cluster ($z = 0.024$) in a distance modulus of d$m = 35.10$ mag, for the cluster A 2218 ($z = 0.175$) in d$m = 39.64$ mag and for A 2390 ($z = 0.228$) in d$m = 40.28$ mag, a scale of 3.65 kpc arcsec^{-1} and a lookback time of ∼2.75 Gyr.

2 PHOTOMETRY OF ABELL 2390

2.1 Abell 2390

The cluster Abell 2390 ($\alpha_{2000} = 21^{\rm h}53^{\rm m}34\overset{\rm s}{.}6$, $\delta_{2000} = +17^\circ 40' 10\overset{''}{.}9$) at $z = 0.228$, richness class 1, has a large velocity dispersion, $\sigma = 1100 \pm 63$ km s^{-1} (Carlberg et al. 1996) and a high X-ray luminosity, $L_{\rm X}(0.7\text{–}3.5\ {\rm keV}) = 4.7 \times 10^{44}$ erg s^{-1} (Le Borgne et al. 1991). Carlberg et al. (1996) analysed the dynamical state of the cluster and its mass distribution and found a virial radius of $R_{\rm v} = 3.156\, h_{100}^{-1}$ Mpc and virial mass of $M_{\rm v} = 2.6 \times 10^{15}\, h^{-1}\, {\rm M}_\odot$, which makes A 2390 more massive than Coma ($M_{\rm v} = 2.1 \times 10^{15}\, h^{-1}\, {\rm M}_\odot$). At a constant mean interior density of $200\rho_{\rm c}$, A 2390 and Coma have M_{200} masses of 1.2 and $1.3 \times 10^{15}\, h^{-1}\, {\rm M}_\odot$, respectively.

Our study of the early-type galaxy population in A 2390 is based upon multi-object spectroscopy (MOS) using the multi-object spectrograph for Calar Alto (MOSCA) on the Calar Alto 3.5-m Telescope at Calar Alto Observatory (CAHA) in Spain (see Section 3). In addition, optical photometry from the 5.1-m Hale telescope at Palomar Observatory is available and we have exploited WFPC2 images taken with *HST* providing high-quality morphological information for a subset of our sample. Table 1 gives a summary of the observations obtained.

2.2 Ground-based *UBI* imaging

Abell 2390 was observed at the 5.1-m Hale telescope at Mount Palomar using Carnegie Observatories Spectroscopic Multislit and

Table 1. Log of observations.

Tel.	Instrument	Date	Band (phot) Mask/$N_{\rm spec}$	$T_{\rm exp}$ (ks)
HALE	COSMIC	09–12/06/94	*U*	3.00
	COSMIC	09–12/06/94	*B*	0.50
	COSMIC	09–12/06/94	*I*	0.50
HST	WFPC	10/12/94	F555W	8.40
	WFPC	10/12/94	F814W	10.50
CA 3.5	MOSCA	07–10/09/99	1/17	29.88
	MOSCA	07–10/09/99	2/22	42.12
	MOSCA	26–28/07/00	3/24	42.48

Imaging Camera (COSMIC) in the *U* (3000 s), *B* (500 s) and *I* bands (500 s), allowing one to select early-type galaxies in the full FOV of MOSCA due to the nearly equally large FOV of COSMIC (9.7×9.7 arcmin^2). Seeing conditions ranged from 1.4 arcsec in the *U* band, 1.3 arcsec in the *B* band to 1.1 arcsec in the *I* band (Smail et al. 1998). At $I = 22.5$ mag a completeness level of 80 per cent from a comparison with deeper field counts is warranted. All frames from the ground-based imaging data were reduced in a standard manner with IRAF [1] using standard reduction packages.

As a consistency check of our ground-based photometry we compared our photometric data with the results for the cluster A 2390 by Yee et al. (1996) which were derived as part of the CNOC cluster redshift survey. Through a cross-correlation we identified 12 galaxies with spectra that are included in both data sets. After the transformation of our *I* to Gunn *r*-band magnitudes, we found no significant difference between the magnitudes, $\Delta(r - r_{\rm Yee}) = 0.04 \pm 0.16$ mag. In addition, the redshift determinations of all of these objects show a very good agreement.

Absolute magnitudes were calculated from our ground-based *UBI* imaging. Total apparent magnitudes were derived with the Source Extractor package (SEXTRACTOR, see Bertin & Arnouts 1996) as given by MAG_BEST. The transformation of the Johnson–Kron–Cousins *I*-band magnitudes to absolute Gunn *r*-band rest-frame magnitudes was performed in the following way. Synthetic photometry was performed using the observed spectral template for a typical E/S0 galaxy by Kinney et al. (1996) and the synthetic spectral templates by Möller et al. (2001), which were generated with evolutionary synthesis models. The spectral energy distributions (SEDs) were redshifted to the cluster redshift of $z = 0.23$ to determine the flux through the *I* filter and at $z = 0$ through the Thuan & Gunn (1976) *r* filter. This led to the transformation $I_{\rm obs} - {\rm Gunn}\, r_{\rm rest} = -0.81$. Typical uncertainties in the *k*-corrections are $\Delta k_r = 0.03$ mag for the SEDs of both ellipticals and S0 galaxies.

The correction for the Galactic extinction was performed using the *COBE* dust maps of Schlegel, Finkbeiner & Davis (1998). For A 2390 an index $E(B - V) = 0.110$ mag was determined, resulting in extinction coefficients for the Johnson Cousins filters of $A_U = 0.600$ mag, $A_B = 0.476$ mag and $A_I = 0.214$ mag, respectively. For the *HST*/*WFPC2* F814W filter $A_{814} = 0.214$ mag was derived. The uncertainty in the extinction is $E(B - V) = 0.010$ mag.

The total errors in absolute magnitude Gunn *r* band, $\delta\sigma_{M_r}$, follow as the linear sum of the errors in the total *I*-band magnitude $\delta\sigma_I$, the uncertainty in the *k*-correction $\delta\sigma_{k_r}$ and the error in the extinction correction $\delta\sigma_{A_I}$. For our ground-based magnitudes $\delta\sigma_{M_r}$ covers the range between $0.07 \leqslant \delta\sigma_{M_r} \leqslant 0.14$ mag, with an average error of $\delta\overline{\sigma}_{M_r} = 0.09$ mag.

2.3 Structural parameters

During Cycle 4 A 2390 was observed with the *HST*[2] in the filter F555W (V_{555}) with 8400 s and in the F814W (I_{814}) with 10 500 s as part of a large gravitational lensing survey. These exposure times are deep enough to determine structural parameters down to $B_{\rm rest} \sim 23$ mag (Ziegler et al. 1999).

2.3.1 Choice of luminosity profile

A fundamental question when determining the structural parameters of galaxies is what kind of surface brightness profile type is the most suitable. Generally, derivation of total magnitudes involves an extrapolation of curves of growth to infinity, thus relying on fits to the luminosity profiles of the galaxies. For example, Caon, Capaccioli & D'Onofrio (1993) used Sérsic profiles to fit the surface brightness profile of early-type galaxies (see also La Barbera et al. 2002). Another approach is to use the classical de Vaucouleurs ($r^{1/4}$) law with an exponential disc component (e.g. Simard et al. 2002; Tran et al. 2003).

Tran et al. (2003) explored the results of three different profile models (double exponential, Sérsic bulge+exponential disc and an $r^{1/4}$ bulge+exponential disc) using the galaxy image two-dimensional (2D) package (GIM2D, Simard et al. 2002) on a sample of 155 cluster galaxies in CL 1358+62 at $z = 0.33$. Based on their extensive profile tests these authors conclude that the de Vaucouleurs bulge with an exponential disc profile is the most appropriate way of investigating the structural properties. As our sample comprises only early-type galaxies we use a similar approach, namely a combination of an $r^{1/4}$ plus exponential disc profile by Saglia et al. (1997a). These authors demonstrated that the Sérsic $r^{1/n}$ profiles can be understood as a 'subset' of $r^{1/4}$+exponential models. This algorithm also explores the effect of an efficient sky subtraction. For example, for $n > 4$ large extrapolations are needed which could lead to large errors in the sky subtraction of up to ± 3 per cent and, therefore, to additional uncertainties in the absolute magnitudes and half-light radii.

2.3.2 The surface brightness models

For analysing structural parameters we use the fitting algorithm developed by Saglia et al. (1997a,b). The parameters of the galaxies are derived by searching for the best combination of seeing-convolved, sky-corrected $r^{1/4}$ and exponential laws. This approach accounts for various types of observed luminosity profiles, i.e. it models the extended luminosity profiles of cD galaxies and provides fits to the range of profile shapes of early-type galaxies (ellipticals featuring a flat core to S0 galaxies with the presence of a prominent disc).

Subframes of all 14 early-type galaxies both with spectroscopic and *HST* information (without the cD galaxy) were extracted and each galaxy was analysed individually. In a first step stars and artefacts around the galaxies were masked in order not to cause any problems in the fitting process. In the next step the circularly averaged surface brightness profile of the galaxy was fitted with point spread function convolved $r^{1/4}$ and exponential components, both simultaneously and separately (see also Z01; Fritz et al. 2004). This

[1] IRAF is distributed by the National Optical Astronomy Observatories, which are operated by the Association of Universities for Research in Astronomy, Inc., under cooperative agreement with the National Science Foundation.

[2] Based on observations made with the NASA/ESA *Hubble Space Telescope*, obtained at the Space Telescope Science Institute, which is operated by the Association of Universities for Research in Astronomy, Inc., under NASA contract NAS 5-26555. These observations are associated with programme no 5352.

method allows one to derive the effective (half-light) radius R_e (in arcsec), the total F814W-band magnitude I_{814} and the mean surface brightness within R_e, $\langle\mu_e\rangle$, for the entire galaxy as well as the luminosity and scale of the bulge (m_b and $R_{e,b}$) and disc (m_d and h) component separately, within the limitations described by Saglia et al. (1997a).

In total, structural parameters could be determined for 14 galaxies out of 15 for which we also have obtained spectra (see Table 2). In Fig. A1 of Appendix A examples of the surface brightness profile fits are shown. In most cases, the observed profile is best described by a combination of a bulge (de Vaucouleurs law) and a disc component (exponential law). Typical residuals $\Delta\mu_I$ between the observed profile and the fit as a function of $R^{1/4}$ are of the order of $0.01 \leqslant \Delta\mu_I \leqslant 0.10$ mag. Comparing the differences between elliptical and lenticular (S0) galaxies we detect a small disc component for the S0s exhibiting a lens-like structure. For example, the elliptical galaxy no 2438 is well represented by a pure de Vaucouleurs profile. In the case of the S0 galaxy no 2946 a combined model of an $R^{1/4}$ law and an additional disc component results in the best luminosity profile. For the innermost regions ($R^{1/4} \lesssim 0.5$), the model is extrapolated to the calculated central surface brightness μ_0 of the galaxy.

For some cases (nos 2198, 2438 and 2763) we do not detect any additional disc component, i.e. a pure classical de Vaucouleurs law profile ($D/B = 0$) results in the best profile for the light distribution of the galaxy. Therefore, our approach also allows for the possibility that dynamically hot galaxies may all have $r^{1/4}$ profiles. However, most of our galaxies are well described by the superposition of $r^{1/4}$ bulge and exponential disc profiles. Bulge+disc models provide better fits than a pure $r^{1/4}$ law, and the addition of an exponential disc component improves the fit for many of the galaxies. The surface brightness at the half-light radius is a strong function of the chosen fitting profile and the half-light radius is dependent on the assumed surface brightness model. However, the product $R_e \langle I_e\rangle^\beta$ (with $\beta \simeq 0.8$) provides a FP parameter which is stable for *all* applied profile types, from $r^{1/4}$ to exponential laws (Saglia, Bender & Dressler 1993; Kelson et al. 2000a). Under the constraint of this coupling, galaxies can only move parallel to the edge-on view of the FP.

Some previous FP studies derived their structural parameters with a pure $r^{1/4}$ profile. Therefore, we have also tested our results using surface brightness models based on a pure de Vaucouleurs law only. Only systems featuring a dominant disc (Sa bulges) show some deviations. As expected, these galaxies move only along the edge-on projection of the FP. Note, that the errors of the FP parameters of effective radius (R_e) and surface brightness (μ_e) are highly correlated. However, the rms uncertainty in the product $R_e\, I_e^{0.8}$ which propagates into the FP is only ≈4 per cent, corresponding to $\Delta\mu_e = \beta\Delta\log R_e$ with $\beta = 0.328$ and a scatter of the latter relation of 0.05 mag arcsec^{-2} (Saglia et al. 1993). The results of the $r^{1/4}$ structural measurements are presented in Table 3. Fig. 8 (below) shows the FP for A 2218 and A2390 constructed based on a pure $r^{1/4}$-law profile. The $r^{1/4}$-law structural parameters for A 2218 can be requested from the first author.

Thumbnail images for the 14 galaxies are provided in Appendix A in Fig. A2. A detailed description of the morphological classification of galaxies residing in the *HST* field is outlined in Appendix A. The final classification is listed in Table 2 and is also given for each galaxy in Fig. A2.

As an additional comparison, we also performed an isophote analysis based on the procedure introduced by Bender & Möllenhoff (1987). Deviations from the elliptical isophotes were recorded as a function of radius by a Fourier decomposition algorithm. The presence and strength of the a_4 coefficient, which represents the signature of diskyness, is in good agreement with the visually classified morphologies of S0 and spiral bulges.

2.3.3 Error evaluation

The errors of the photometric parameters of effective radius and surface brightness are correlated and enter the FP in combination. The errors in R_e (in arcsec) and μ_e (in magnitudes) propagate into the FP relationship in the following form (Treu et al. 2001a):

$$\delta FP_{\rm phot} = \log \delta R_e - \beta\delta\mu_e. \quad (1)$$

An error calculation using this formula is not an approximation but a particularly robust computation, as in three-dimensional space

Table 2. Galaxy properties of the *HST* subsample.

ID	σ_c (km s^{-1})	I_{814} (mag)	$\langle\mu_e\rangle_r$ (mag arcsec^{-2})	M_r (mag)	R_e (arcsec)	log R_e (kpc)	$R_{e,b}$ (arcsec)	$R_e I_e^{0.8}$	h (arcsec)	D/B	Morp
(1)	(2)	(3)	(4)	(5)	(6)	(7)	(8)	(9)	(10)	(11)	(12)
2106	144.5 ± 16.8	19.18	18.28	19.93	0.282	0.013	0.250	0.033	0.20	0.36	E
2120	140.3 ± 15.3	18.88	18.22	19.63	0.314	0.060	0.202	0.154	0.34	0.46	S0
2138	165.4 ± 08.7	16.97	20.60	17.72	2.264	0.918	1.324	1.800	4.48	0.36	E
2180	161.2 ± 10.6	17.80	19.49	18.55	0.928	0.530	0.580	1.195	0.88	0.60	S0
2198	148.9 ± 15.6	18.59	17.92	19.34	0.313	0.058	0.313	0.155	0.00	0.00	E
2237	162.2 ± 12.3	17.66	19.94	18.41	1.217	0.648	1.195	1.385	0.73	0.81	Sa
2438	119.8 ± 15.9	18.74	19.59	19.49	0.631	0.363	0.631	0.808	0.00	0.00	E
2460	258.6 ± 10.2	18.00	18.90	18.75	0.642	0.370	0.509	0.892	1.09	0.17	E
2592	192.0 ± 11.4	17.20	20.11	17.95	1.625	0.774	1.104	1.618	2.55	0.29	E
2619	229.3 ± 14.3	18.53	18.20	19.28	0.366	0.126	0.320	0.326	0.27	0.37	E
2626	195.6 ± 12.7	18.31	18.65	19.06	0.497	0.259	0.325	0.640	0.38	0.92	S0
2763	300.5 ± 12.2	17.55	18.89	18.30	0.789	0.460	0.789	1.108	0.00	0.00	E
2946	131.9 ± 15.2	18.69	19.26	19.44	0.554	0.306	0.405	0.708	0.60	0.34	S0
6666	211.0 ± 13.5	17.65	18.79	18.40	0.721	0.421	0.488	1.024	1.00	0.32	E/S0

Notes: (1) Galaxy ID, (2) velocity dispersion σ_c (aperture-corrected) with errors (in km s^{-1}), (3) extinction-corrected, Vega-based total magnitude in WFPC2 F814W filter, (4) mean surface brightness magnitude $\langle\mu_e\rangle$ in Gunn r band corrected for cosmic expansion, (5) rest-frame Gunn r-band magnitude (in mag), (6) effective radius (in arcsec) and (7) effective radius (in kpc), (8) effective radius of the bulge (in arcsec), (9) FP parameter $R_e\, I_e^{0.8}$, (10) disc scalelength (in arcsec), (11) disc-to-bulge ratio and (12) morphology of the object.

Table 3. Galaxy parameters of the *HST* subsample based on pure de Vaucouleurs surface brightness fits. Columns are tabulated analogously to Table 2. The velocity dispersions σ with corresponding errors (in km s^{-1}) are not aperture-corrected.

ID	σ (km s^{-1})	I_{814} (mag)	$\langle\mu_e\rangle_r$ (mag arcsec^{-2})	M_r (mag)	R_e (arcsec)	log R_e (kpc)	$R_{e,b}$ (arcsec)	$R_e I_e^{0.8}$
(1)	(2)	(3)	(4)	(5)	(6)	(7)	(8)	(9)
2106	131.0 ± 16.8	19.07	18.55	19.82	0.335	0.088	0.335	0.219
2120	127.2 ± 15.3	18.75	18.51	19.50	0.382	0.145	0.382	0.363
2138	150.0 ± 08.7	17.14	20.04	17.89	1.621	0.772	1.621	1.630
2180	146.2 ± 10.6	17.67	19.79	18.42	1.133	0.617	1.133	1.342
2198	135.0 ± 15.6	18.59	17.92	19.34	0.313	0.058	0.313	0.155
2237	147.1 ± 12.3	17.12	21.10	17.87	2.667	0.989	2.667	1.802
2438	108.6 ± 15.9	18.74	19.59	19.49	0.631	0.363	0.631	0.808
2460	234.5 ± 10.2	18.01	18.86	18.76	0.628	0.361	0.628	0.872
2592	174.1 ± 11.4	17.27	19.87	18.02	1.408	0.711	1.408	1.533
2619	207.9 ± 14.3	18.40	18.55	19.15	0.456	0.222	0.456	0.553
2626	177.4 ± 12.7	18.01	19.29	18.76	0.768	0.448	0.768	1.033
2763	272.5 ± 12.2	17.55	18.89	18.30	0.789	0.460	0.789	1.108
2946	119.6 ± 15.2	18.62	19.36	19.37	0.599	0.340	0.599	0.778
6666	191.3 ± 13.5	17.65	18.74	18.40	0.701	0.408	0.701	1.000

defined by the FP it is the only natural way to provide an accurate error estimation (see also Saglia et al. 1997a; Kelson et al. 2000a; Treu et al. 2001a for further details). For this reason, we show the errors in the FP only in the edge-on projection along the short axis that separates kinematic measurements and photometric parameters (see the upper right-hand panel in Fig. 7, below). The errors are calculated for the F814W filter with a parameter value of $\beta = 0.328$. As the slope β is very well defined with only a small variation with wavelength, the error estimations change negligibly within the observed range of β values (Pahre, Djorgovski & de Carvalho 1998).

The errors on the derived structural parameters are assigned through a combination of individual quality parameters, including the effects of sky subtraction errors, seeing and pixel sampling, average galaxy surface brightness relative to the sky, signal-to-noise (S/N) ratio variations, extrapolation involved to derive M_{tot}, the radial extent of the profile and the reduced χ^2 of the fit resulting in a final global quality parameter. The total quality parameter Q is defined by the maximum of the quality parameters of individual errors $Q = \max(Q_{max}, Q_\Gamma, Q_{S/N}, Q_{sky}, Q_{\delta sky}, Q_E, Q_{\chi^2})$ (Saglia et al. 1997a). For $Q = 1$ the typical uncertainty in total magnitude is $\Delta M_{tot} = 0.05$ and in effective radius $\Delta \log R_e = 0.04$ (<10 per cent). A value of $Q = 2$ leads to errors of $\Delta M_{tot} = 0.15$ and $\Delta \log R_e = 0.1$ (<25 per cent), respectively. A quality parameter of $Q = 3$ ensues errors of $\Delta M_{tot} = 0.4$ and $\Delta \log R_e = 0.3$. For A 2390 we find that 43 per cent (6) of our galaxies have $Q = 1$, 57 per cent (8) galaxies have $Q = 2$ and no galaxy yields a quality parameter of $Q = 3$. We estimate the average error in I_{814} to be ≈10 per cent and the error in R_e to be <25 per cent.

Furthermore, we include variations in the zero-point calibration of $\delta ZP = 0.03$ (Saglia et al. 1997b), an uncertainty in the galactic extinction of $\delta E(B - V) = 0.010$ and errors in the k-correction of $\delta m_r = 0.02$ mag. The combination of the uncertainties on the measured parameters $\delta\mu_e$ (in mag) and $\log \delta R_e$ (in arcsec) according to equation (1) are listed as δFP_{phot}. Adding the errors of galactic extinction correction, the k-correction and the errors in the zero-point in quadrature gives the final total error of the FP in the rest-frame Gunn r band, δFP_r. A summary of our error analysis is given in Table 4.

2.3.4 *Determination of rest-frame surface brightnesses*

At the cluster redshift of A 2390, the observed F814W passband is close to the rest-frame Gunn r_{rest}. Therefore, it is more promising to use a single k-correction term of the observed I_{814} to Gunn r band in the rest frame rather than to take the more complicated route of converting to R_c first and then using a colour transformation. The latter procedure would increase the overall uncertainties.

Analysis of the rest-frame luminosities of the galaxies was performed in the following way. According to Holtzman et al. (1995), the instrumental magnitude in the F814W filter is given by

$$I_{814} = -2.5 \log(\mathrm{DN})/t_{exp} + ZP + 2.5 \log(GR) \quad (2)$$

with GR being the respective gain ratios for the WF chips and ZP the zero-point for an exposure time $t_{exp} = 1$ s. $ZP = 20.986$ with consideration of the difference between 'short' and 'long' exposures of 0.05 mag (Hill et al. 1998) and an aperture correction of 0.0983 (Holtzman et al. 1995).

As we do not have any ground-based $V - I$ colours a similar transformation from Cousins I to Gunn r band following the procedure as in Z01 cannot be conducted. Instead, we used the spectral template for a typical E/S0 galaxy by Kinney et al. (1996), redshifting it to the cluster redshift of $z = 0.23$, to determine the flux through the I_{814} filter and at $z = 0$ through the Thuan & Gunn (1976) r filter. This led to the translation $I_{814\,obs} - \mathrm{Gunn}\,r_{rest} =$

Table 4. Error analysis for the FP. The total error on the combination that enters the FP, $\delta FP_{phot} = \log \delta R_e - \beta\, \delta\mu_e$ (see equation 1) is listed as δFP_{phot}, adopting $\beta = 0.328$. The final FP error in the rest-frame properties is given in the column δFP_r.

ID	$\delta\mu_e$	$\log \delta R_e$	δFP_{phot}	δFP_r
2106	0.078	−0.055	0.081	0.082
2120	0.071	−0.020	0.044	0.045
2138	0.136	0.124	0.080	0.081
2180	0.049	−0.001	0.017	0.019
2198	0.073	−0.020	0.044	0.046
2237	0.076	0.050	0.025	0.027
2438	0.027	−0.040	0.049	0.051
2460	0.030	−0.019	0.029	0.031
2592	0.105	0.094	0.059	0.061
2619	0.054	−0.018	0.035	0.037
2626	0.029	−0.030	0.040	0.041
2763	0.032	−0.004	0.015	0.016
2946	0.021	−0.026	0.033	0.034
6666	0.028	−0.014	0.023	0.025

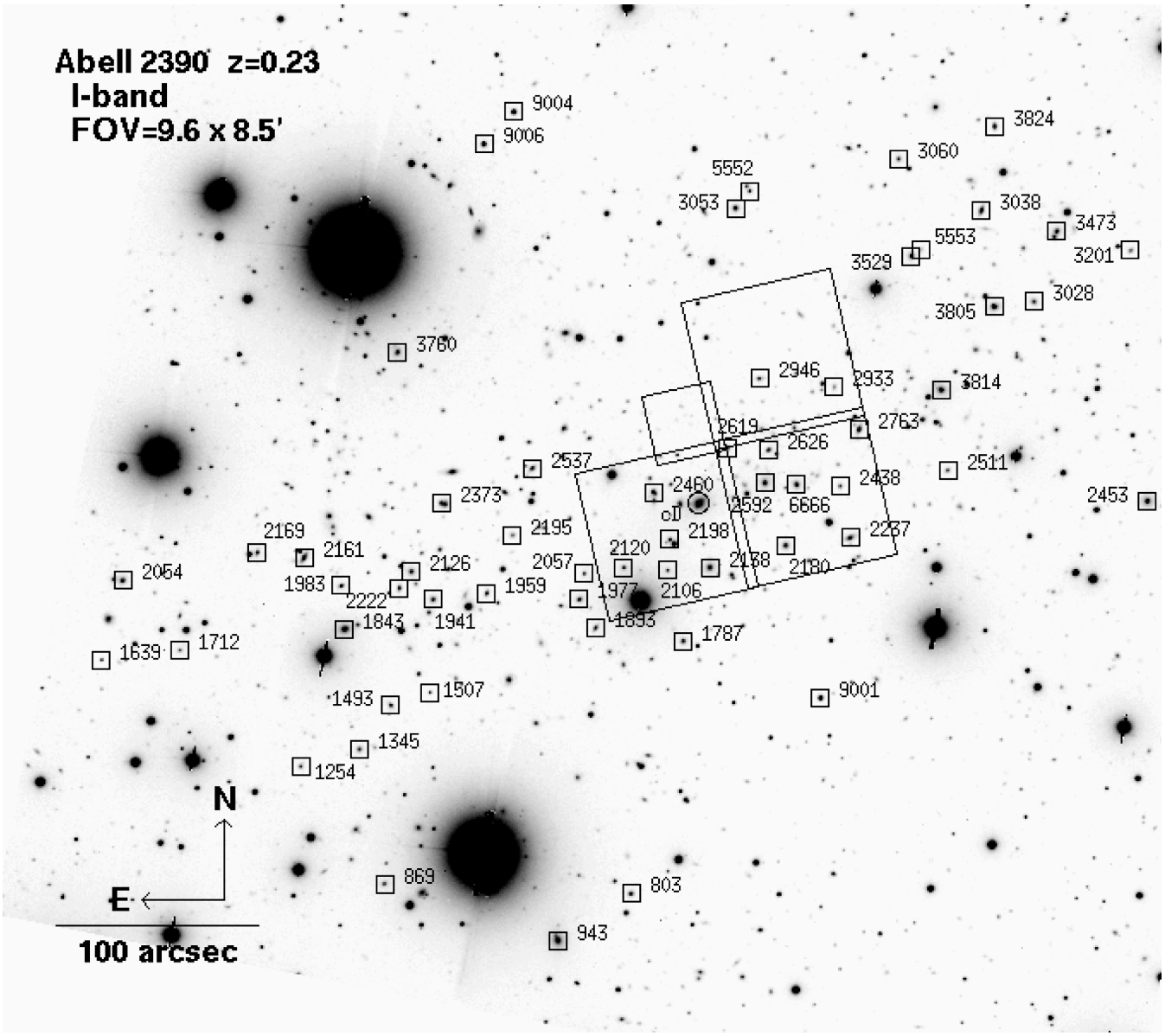

Figure 1. *I*-band image of the cluster Abell 2390 at $z = 0.23$, taken with the 5.1-m Hale telescope on Mt Palomar. The total FOV is 9.6×8.5 arcmin^2. North is up and east to the left. The length of the scale bar in the left-hand corner corresponds to 100 arcsec, or 365 kpc at the distance of A 2390 ($\Omega_m = 0.3$, $\Omega_\Lambda = 0.7$, h_{70}^{-1}). Galaxies with spectra are indicated by squares. The cD galaxy is marked with a circle. Stars used for the mask alignment are labelled as ID = 900x. An overlay of the *HST* WFPC2 FOV is also indicated.

-0.75. We checked this result by transforming the synthetic SEDs using Möller et al. (2001), yielding only a slightly higher value of 0.02 mag.

The mean surface brightness within R_e is defined as

$$\langle \mu_r \rangle_e = r_{\rm rest} + 2.5 \log(2\pi) + 5 \log(R_e) - 10 \log(1+z), \quad (3)$$

where the parameter $r_{\rm rest}$ denotes the rest-frame Gunn r-band magnitude. The dimming due to the expansion of the Universe is corrected by the final term of this equation. Applying the formula in Z01, the mean surface brightness $\langle I \rangle_e$ in units of $L_\odot$ pc^{-2} was calculated. Furthermore, the effective radius in kpc was computed for our cosmology with an angular distance of A 2390 of $d = 753.41$ Mpc. For Coma ($z = 0.024$) the angular distance is $d = 99.90$ Mpc.

3 SPECTROSCOPY OF ABELL 2390

3.1 Sample selection

In order to enable a good sky subtraction which requires long slit lengths (with a minimum length of 15 arcsec), each mask was constrained to only approximately 20 galaxies in total. For this reason, we were very careful to select only galaxies which were likely to be cluster members based upon their *UBI* broad-band colours. The target objects were selected on the basis of the ground-based *I*-band images and a combination of defined colour regions. Using a similar selection procedure as described in Z01, all galaxies were rejected that fall outside a defined colour range, restricted to $2.60 < (B - I) < 3.50$ and $-0.2 < (U - B) < 0.40$. This method sets negligible restrictions on the stellar populations of the selected objects, but

eliminates the majority of background galaxies. As our galaxies were distributed over the whole FOV of $\sim$10 $\times$ 10 arcmin^2 (see Fig. 1), corresponding to $1.53 \times 1.53\,h_{70}^{-2}$ Mpc^2, we can study the evolution of early-type galaxies out to large clustercentric distances.

3.2 Observations

The observations were carried out during two observing runs over four nights (1999 September 7–11) and five nights (2000 July 26–31). To achieve intermediate resolution spectra for the galaxies in A 2390 at $z = 0.23$, we chose the grism GREEN 1000 with a typical wavelength range of $\lambda = 4500$–7500 Å, encompassing important absorption lines such as Hγ, Hβ, Mg$_b$, Fe5270 and Fe5335 at the cluster redshift of $z = 0.228$. The slit widths were set to 1.5 arcsec and the instrumental resolution around Hβ and Mg$_b$ ($5900 \lesssim \lambda_{\rm obs} \lesssim 6400$ Å) was 5.5 Å FWHM, corresponding to $\sigma_{\rm inst} \sim 100$ km s^{-1}. The spatial scale was 0.33 arcsec pixel^{-1} and seeing conditions varied between $1.2 \leqslant {\rm FWHM} \leqslant 1.7$ arcsec.

Three masks were observed with total exposure times of between 29 880 s (8.3 h) and 42 480 s (11.8 h) each (see Table 1). In total, we obtained 63 high signal-to-noise spectra of 52 different galaxies, of which 15 are situated within the *HST* field. Three objects, nos 1507, 1639 and 2933, turned out to be background galaxies at $z = 0.3275$, 0.3249 and 0.3981, respectively; one galaxy (no 3038) is located in the foreground at $z = 0.1798$. We discard these galaxies from our sample, yielding a total of 48 different early-type cluster members, proving that our sample selection was highly efficient.

In Fig. 2 the colour–magnitude diagram $(B - I)$ versus I for our 48 early-type cluster members of A 2390 with available spectroscopic information is shown. A least-squares fit to the seven ellipticals in A 2390 gives $(B - I)_{\rm E} = -0.011(I_{\rm tot}) + 3.405$, which is indicated by the solid line in Fig. 2. The outlier object no 2237 with the bluest colour of $(B - I) = 2.77$ was classified as a spiral Sa galaxy.

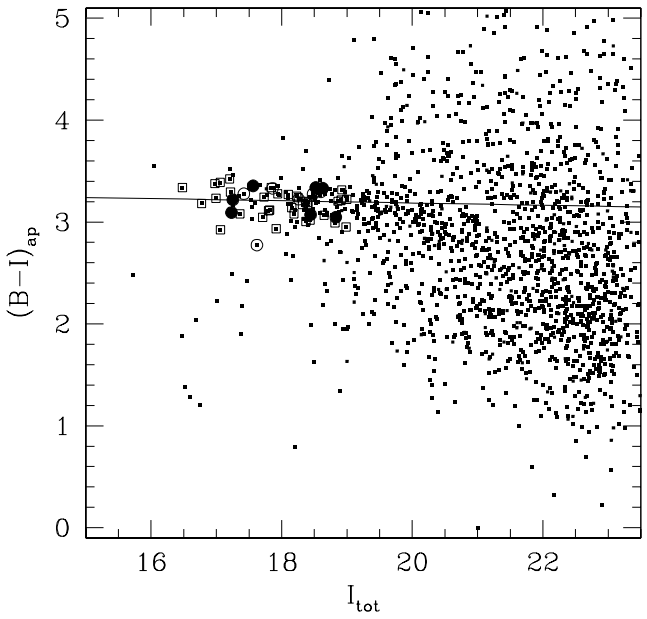

Figure 2. $(B - I) - I$ colour–magnitude diagram for galaxies brighter than $I = 23.5$ mag, obtained from our HALE imaging and the 48 observed early-type cluster members of A 2390 with available spectra (squares). Circles represent those galaxies in A 2390 which enter the FP, ellipticals (filled circles) and S0 galaxies (open circles). The solid line is a least-squares fit to seven ellipticals.

3.3 Data reduction

The reduction of the spectra was undertaken using MIDAS[3] with our own FORTRAN routines and followed the standard procedure. For each observing run, bias frames were taken at the beginning and end of the night. All frames showed a very stable two-dimensional structure, thus all bias frames from the individual nights were used to generate master biases, one for each observing run. An averaged superbias image was constructed from median-scaled individual bias frames. After calculating the median in the overscan region of the superbias, the superbias frame was scaled to the median of each individual bias image. Finally, this scaled master bias frame was subtracted from each frame. Variations in the bias level were $\leqslant$5 per cent.

The 2D images of each slit spectrum were extracted from the MOS frame (after bias subtraction) and reduced individually. Special care was taken in correcting for the S-distortions (curvature) of the spectra, which were strongest when lying closest to the edges of the field. For this purpose a special IRAF program was used which fits a user-defined Legendre polynomial (in most cases of third order) to compute the parameters for the curvature correction. The same set of coefficients were applied to the science, flat-field and corresponding wavelength calibration frames, respectively.

A minimum number of five dome flat-fields were used to construct a master flat-field through a combination of median-averaged single flat-field exposures. After the rectification, the flat-field slit exposures were approximated by a spline function of third degree to the continuum of each spectrum (in dispersion direction) to account for the CCD response curve. The smoothed spline fit was then applied for normalization of the original flat-field frame in order to correct for pixel-to-pixel variations.

Cosmic ray events were removed very careful by a $\kappa - \sigma$ clipping algorithm with a 5 $\times$ 5 pixel filter, taking then into account only to eliminate possible artefacts in the spectra. Furthermore, up to five bad columns per slitlet were cleaned by interpolating from unaffected adjacent columns.

The sky background was subtracted by iteratively fitting each CCD column separately through a $\kappa - \sigma$ clipping algorithm. To ensure consistent profile centres to within at least half a pixel, corresponding to 0.17 arcsec, the one-dimensional spectra were extracted for each exposure separately using the Horne algorithm (Horne 1986), which optimally weights the extracted profile to maximize the signal-to-noise ratio. Thus, possible shifts of the spectra which may have occurred during different nights are accounted for in the final one-dimensional summed-up spectra.

For the wavelength calibration exposures, the HgAr and Ne lamps were switched on together in order to gain a sufficient number of emission lines over a large range, $\lambda \approx 5450$–7450 Å. A two-dimensional dispersion relation was computed using polynomial fit functions of third and second degree in dispersion and in spatial direction, respectively. Typical rms errors of the dispersion fit were 0.05–0.06 Å at a stepsize of 1.3 Å pixel^{-1}. After the wavelength calibration, individual exposures were summed and the final one-dimensional spectrum (see Fig. 3) was rebinned to logarithmic wavelength steps in preparation for the determination of the velocity dispersion using the Fourier correlation quotient (FCQ) method (Bender 1990) and measurement of absorption-line strengths.

[3] ESO–MIDAS, the European Southern Observatory Munich Image Data Analysis System is developed and maintained by the European Southern Observatory.

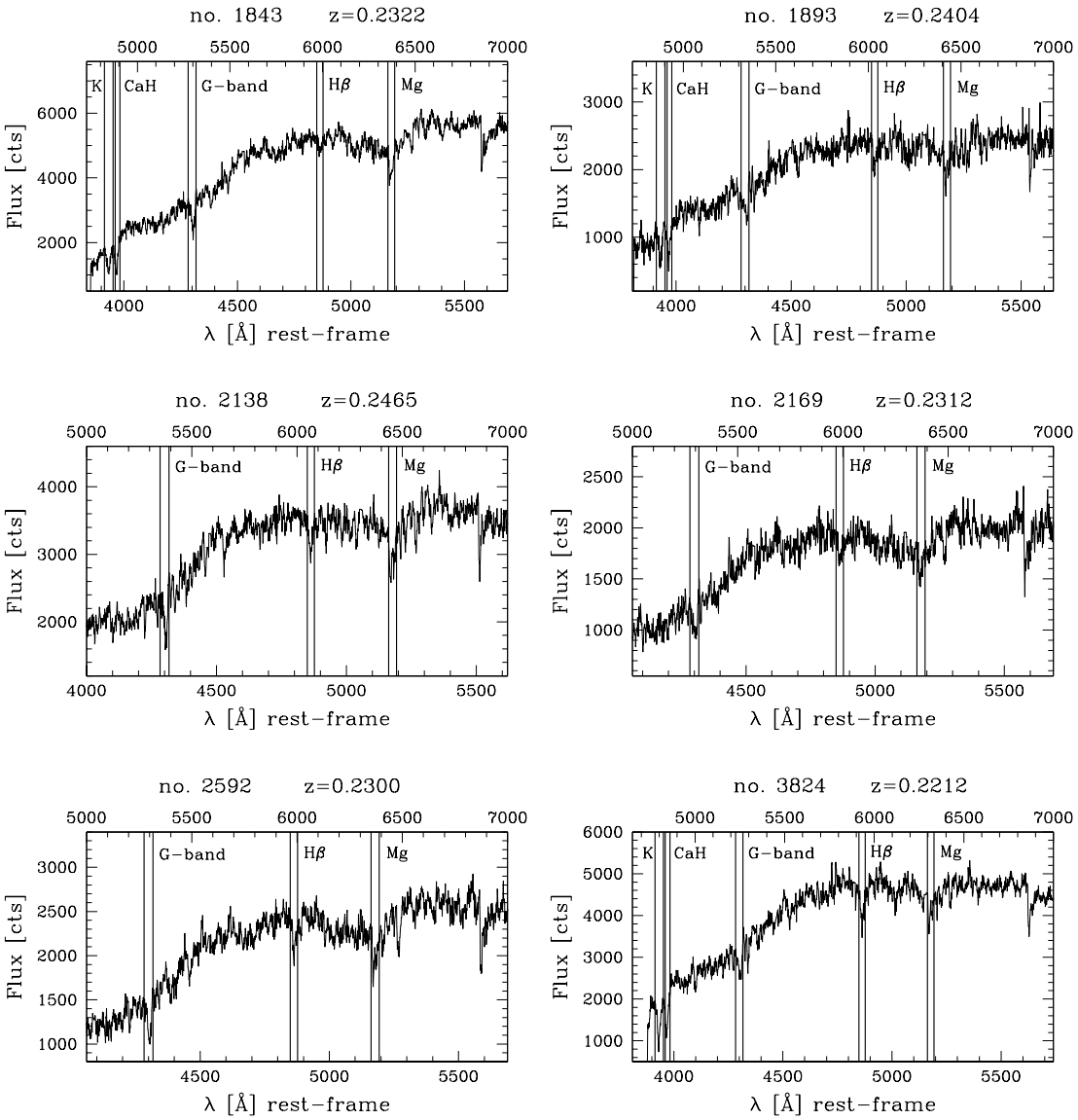

Figure 3. Example spectra (not flux-calibrated) of early-type galaxies in our sample. The lower x-axis represents the rest-frame wavelengths and the upper one the observed wavelengths (both in Å). The ordinate gives the flux in counts (1 ADU = 1.1 e^{-1}). Prominent absorption features are marked and the ID and the determined redshift are given above each panel.

In a similar manner, the spectra of standard stars were reduced. Two spectrophotometric flux standards (HZ2 and HZ4) were observed through an acquisition star hole in one mask. For the kinematic templates, three K giant stars [SAO 32042 (K3III), SAO 80333 (K0III), SAO 98087 (K0III)] were observed through a 0.5-arcsec long slit using the same grism as for the galaxies. These stars had a spectral resolution at Hβ and Mg$_b$ of $\sim$2.2 Å FWHM (corresponding to $\sigma_* = 55$ km s^{-1}). To minimize the effect of any possible variation in slit width, the star spectra were averaged over a small number of rows only.

3.3.1 Velocity dispersions

Galaxy velocity dispersions and radial velocities were calculated using an updated version of the FCQ program kindly provided by Professor R. Bender (Bender 1990). At a redshift of $z = 0.231$ the Mg$_b$ line is strongly affected by the telluric emission line at $\lambda = 6367$ Å. For this reason, two separate wavelength regimes were analysed. The first wavelength range between $\lambda = 6204$ and 6748 Å was centred on the Mg$_b$ feature. In those cases where the Mg$_b$ line was affected, either in the central or in the adjacent continuum windows, a reliable measurement of the velocity dispersion could not be ensured so that a second calculation in the range around the G4300 band between $\lambda = 4964$ and 5541 Å was performed.

As the slitlets of the galaxies had small variations in width size and were not identical in width to the long slit of the stars, a simple comparison and interpretation of the calculated velocity dispersions would be wrong. Thus, we applied a correction procedure to the resulting dispersions to correct for this effect. In a first step, the instrumental dispersion was determined by measuring the width of four unblended emission lines around the position of the redshifted Mg$_b$ in the respective arc spectrum of a galaxy. Typical instrumental resolutions are in the range of $\sigma_{\rm inst} \sim 90$–100 km s^{-1}. The spectra of the stars were broadened to the same resolution (in km s^{-1}) as

the galaxies, before using them as templates in the FCQ algorithm to compute the velocity dispersion for each galaxy. This procedure has the advantage that the galaxy velocity dispersion results directly and no additional correction for the velocity dispersion of the template star $\sigma_{\rm star}$ is needed (see Z01 for an alternative approach). All values of $\sigma_{\rm gal}$ are given in Table B1 in Appendix B together with their corresponding heliocentric radial velocities v.

For a total of eight galaxies which are included in two different MOS masks, we are able to confirm the internal reliability of our spectral analysis. The velocity dispersions have been measured for both individual setups and the agreement between these two determinations is good (with a median offset for σ at the 10 per cent level). In order to increase the signal-to-noise ratio in our final spectra, these repeat observations have been co-added. The S/N ratio in the final spectra varies between 21 and 65 with a median value of S/N $\sim$ 34 Å^{-1} and a mean value of S/N $\sim$ 37 Å^{-1}.

Velocity dispersions were aperture-corrected according to the method outlined by Mehlert et al. (2003). This aperture correction is slightly steeper than that proposed by Jørgensen (1999) (but consistent within the errors). For our σ measurements this results in corrections for the cluster A 2390 of $\Delta(\log\sigma_{\rm A\,2390}) = +0.042$ and the cluster A 2218 of $\Delta(\log\sigma_{\rm A\,2218}) = +0.039$. For A 2390, the aperture radius a was taken as the square root of the slit width of 1.5 arcsec times the mean of number of rows over which the spectra were summed up as 8.4 pixel (corresponding to 2.8 arcsec). More details on the correction method are described in Z01.

4 COMPARISON A 2390 VERSUS A 2218

In a recent study, Z01 performed a detailed analysis of a sample of 48 early-type galaxies in the rich cluster A 2218 at a redshift of $z = 0.18$. Combining this work with our sample of $N = 48$ in A 2390 offers the possibility to explore the evolution of $\sim$100 early-type galaxies over a large luminosity range and a wide FOV at similar cosmic epochs. The combined sample allows an extensive investigation of the evolutionary status of galaxies in rich clusters at $z \sim 0.2$. A subsample with accurate structural parameters provided by *HST* comprises 34 E+S0 galaxies, split into 17 ellipticals (E), two E/S0, nine S0, three SB0/a, two Sa bulges and one Sab spiral bulge that can be investigated in the FP. With this large sample, possible radial and environmental dependences can be explored in detail for the galaxy properties from the cluster centre to the outskirts using the Faber–Jackson relation and for different subpopulations (E/S0 and S0/Sa bulges).

Before the individual galaxies of the two clusters can be combined into one large sample, it has to be proven that both data sets are characterized by very similar properties and that we accounted for possible differences within the subsamples. For this reason, we compare the cluster galaxies with respect to their luminosity, colour, size and velocity dispersion distributions. Both clusters feature similar global cluster properties (e.g. richness class, X-ray luminosity). Furthermore, the sample selection and all observations, especially the spectroscopy, have been carried out in a very similar manner. Therefore, we do not expect significant differences between our galaxy samples.

In the subsequent analysis the cluster galaxies are investigated over the same dynamical range in their properties. Therefore, we excluded the two cD galaxies of the cluster A 2218 as no cD galaxy is included in the A 2390 subsample. A comparison of the cluster properties in absolute rest-frame Gunn r-band magnitude, effective radius, $(B - I)$ rest-frame colour and velocity dispersion (aperture-corrected) is presented in Fig. 4. For each set of parameters, the mean

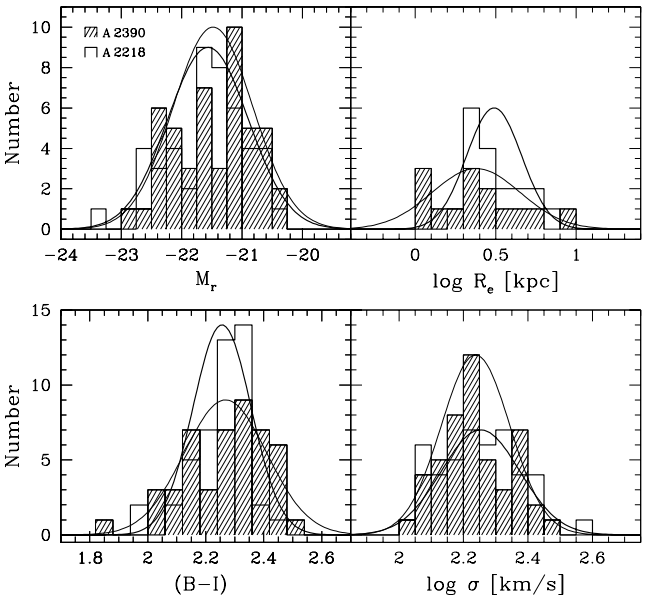

Figure 4. Comparison of galaxy properties. Thin lines and hashed areas represent the distribution for the members in A 2390, solid thick lines the characteristics of the galaxies in A 2218. Gaussian fits showing the mean values with $\pm1\sigma$ scatter are overlayed. Top left: absolute Gunn r-band magnitudes for the whole sample. Top right: size distribution of the *HST* subsample. Bottom left: $(B - I)$ rest-frame colours of member galaxies. Bottom right: distribution of velocity dispersions.

values with the, respectively, $\pm1\sigma$ scatter are indicated as overlayed Gaussian curves. Overall, the galaxies are similarly distributed in all plots. For the galaxies in A 2218 the range of absolute Gunn r-band magnitudes is $-20.50 \geqslant M_r \geqslant -23.42$, for the objects in A 2390 $-20.47 \geqslant M_r \geqslant -22.99$ (upper left-hand panel in Fig. 4). The median value for A 2390 is $\langle M_r\rangle = -21.31$ mag, i.e. 0.17 mag fainter than the median luminosity for the galaxies in A 2218. For the size distribution we consider only the 32 objects within the *HST* fields. In the distributions of galaxy size (upper right-hand panel) small (but not significant) differences are visible. The sizes of the A 2218 galaxies cover a range between 0.22 and 0.82 in $\log R_{\rm e}$ (kpc), with a median of $\log\langle R_{\rm e}\rangle = 0.46$. The A 2390 sample contains more galaxies with smaller effective radii $0.01 \geqslant \log R_{\rm e} \geqslant 0.92$, with a mean of $\overline{\log R_{\rm e}} = 0.38 \pm 0.27$ (and a median of $\log\langle R_{\rm e}\rangle = 0.37$), resulting in a broader distribution than for A 2218. These galaxies are low-luminosity galaxies. We will address this issue in more detail in Section 5.4. The rest-frame colour distributions show no significant differences between the clusters. Using the predictions of passive evolution models by Bruzual & Charlot (1993; GISSEL96 version, hereafter BC96), we corrected for the offset in $\Delta(B - I)$ between the two clusters, which is due to the difference in redshift. The colours of the galaxies in A 2390 cover a range of $1.86 < (B - I) < 2.51$, in A 2218 $1.95 < (B - I) < 2.44$. For the A 2390 galaxies we derive a median value of $\langle(B - I)\rangle = 2.29$, for the A 2218 objects $\langle(B - I)\rangle = 2.28$, respectively. Both are in very good agreement with the typical colour of $(B - I) = 2.27$ for ellipticals at $z = 0$, given by Fukugita, Shimasaku & Ichikawa (1995). The velocity dispersions for the galaxies are equally distributed (lower right-hand panel), with a median value of 165 km s^{-1} [$\overline{\log(\sigma)} = 2.238 \pm 0.11$] for A 2390 and 178 km s^{-1} [$\overline{\log(\sigma)} = 2.253 \pm 0.12$] for A 2218. As the velocity dispersion is an indicator for the mass of an object and the measured σ values exhibit similar ranges, we also conclude that there are no significant differences in mean galaxy masses between the two

samples (see Section 5.5 for a further discussion). In addition, we have also compared the scalelengths (h), disc-to-bulge ratios (D/B) and the surface brightnesses of our member galaxies and again found negligible differences between the distributions.

As a conclusion we detect no significant offset in the distribution of any galaxy parameters between the two samples. Therefore, we conclude that the properties of the galaxies within the two clusters are very homogeneous and thus a combination of the two data sets is adequate, resulting in a final sample of 96 early-type galaxies.

5 RESULTS IN A 2390 AND A2218

In all subsequent figures, large symbols denote the distant galaxies of A2218 and A2390, small boxes represent the local reference sample. Morphologically classified lenticular galaxies (S0) or bulges of early-type spiral galaxies (from the A 2218 and A2390 *HST* fields) are indicated by open symbols, elliptical galaxies are denoted by filled symbols. Both the distant clusters and the local sample are fitted only within the region shown by horizontal and/or vertical dotted lines in the plots, which represent the selection boundaries for the combined A 2218 and A 2390 data. We compare our cluster sample with the local Coma sample by Jørgensen (1999) and Jørgensen, Franx & Kjærgaard (1995). In order to match the selection boundaries for the distant sample, the Coma galaxies were restricted to $M_r < -20.42$ and $\log\sigma > 2.02$. Under the assumption of a non-changing slope, we look at the residuals from the local relation and derive a mean evolution for the distant galaxies.[4]

5.1 Local comparison sample

The Coma cluster at $z = 0.024$ is one of the best studied local rich clusters. Therefore, it provides a reliable local reference when addressing evolutionary questions. Jørgensen (1999) and Jørgensen et al. (1995) (hereafter collectively J99) performed a detailed study of a large number of early-type Coma galaxies in the Gunn r band. The combined sample comprises 115 early-type galaxies, divided into subclasses of 35 E, 55 S0 and 25 intermediate types (E/S0). Absolute magnitudes cover a range down to $M_r < -20.02$ with a completeness level of 93 per cent. In order to match the local J99 sample, the parameters of the distant clusters were aperture-corrected (see Section 3.3). A number of recent works in the literature have analysed the FP at $z > 0.1$ in the Gunn r band and compared it with the Coma cluster (e.g. Jørgensen et al. 1999; Z01). In the intermediate redshift range, observations of early-type galaxies are preferably in the R or I filters. At $z = 0.2$, the observed I and I_{814} passbands are very close to the rest-frame Gunn r band. Therefore, the advantages of using the Gunn r band instead of the bluer Johnson V or B bands are the smaller k-corrections and the lower galactic extinction corrections.

5.2 Faber–Jackson relation

A first test of the formation and evolution of elliptical and lenticular galaxies allows the scaling relation between galaxy luminosity and velocity dispersion, the so-called Faber–Jackson relation (Faber & Jackson 1976). In the B band, the luminosity of an object is proportional to the random motion of the stars as $L \propto \sigma^4$.

[4] For a comparison of the slope of the local and distant galaxies, we use the bisector method, which is a combination of two least-square fits with the dependent and independent variables interchanged. The errors on the bisector fits were evaluated through a bootstrap resampling of the data 100 times.

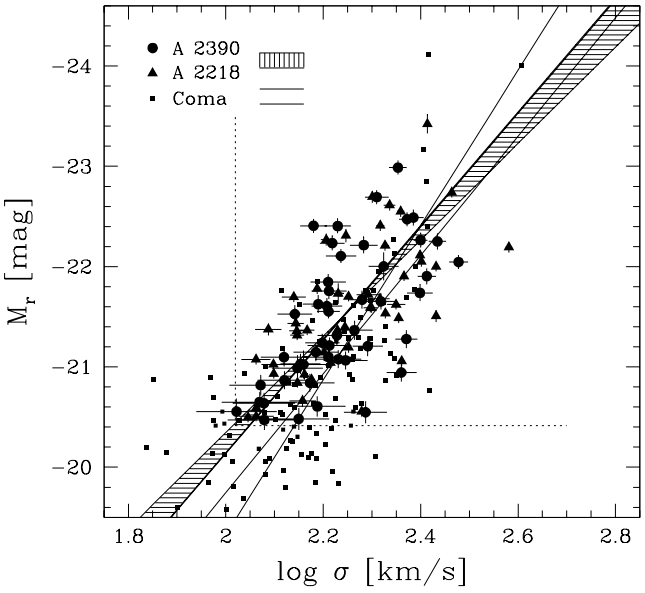

Figure 5. Faber–Jackson relation in Gunn r band for 96 early-type galaxies in A 2390 and A2218, compared with the local Coma sample of J99. The solid lines show the $\pm1\sigma$ errors of the 100 iteration bootstrap bisector fits to the local FJR within selection boundaries, the hashed area indicates the bisector fits to the distant sample (within $\pm1\sigma$).

The Faber–Jackson relation (FJR) in the Gunn r band for 96 distant early-type galaxies in the clusters A 2218 and 2390, compared with the local Coma sample of J99 is shown in Fig. 5. For the FJR scaling relation, the whole cluster data set can be considered as their magnitudes were measured with SEXTRACTOR on the ground-based images. The distant galaxies have velocity dispersions down to 105 km s^{-1}. A bootstrap bisector fit to the restricted Coma reference sample yields

$$M_r = -6.82\log\sigma - 5.90. \quad (4)$$

The observed $\pm1\sigma$ scatter is $\sigma_r = 0.57$ mag. The $\pm1\sigma$ scatter of the bisector fits to the local FJR is indicated as solid lines in Fig. 5. Fits to the distant sample (within $\pm1\sigma$) are shown as the hashed area. Because of the younger mean ages of the stellar populations, the distant clusters are on average brighter than their local counterparts for a given velocity dispersion. If we assume a formation redshift of $z = 2$ for the cluster galaxies, the predictions of single-burst passive evolution models by BC96 (Salpeter IMF with $x = 1.35$, mass range $0.10 < \mathrm{M}_{\odot} < 125.0$ and burst duration of 1 Gyr) suggest an increase of their Gunn r-band brightness by 0.21 ± 0.05 mag at $z = 0.2$. Assuming that the local slope is valid for our distant galaxies, we analyse the mean residuals from the local FJR, i.e. the difference in luminosity for each galaxy from the local FJR fit. The $\pm1\sigma$ scatter of these offsets for the distant galaxies are $\sigma_r = 0.61$ mag.

Table 5 lists the derived mean and median luminosity evolution of our early-type cluster galaxies for various samples in the FJR. The final total error in the FJR evolution results from a linear sum of the total error in absolute magnitude (see Section 2.2) and the error as introduced by the velocity dispersions as $\delta\sigma_M = a\log\delta\sigma_{\mathrm{err}}$, where $\delta\sigma_{\mathrm{err}}$ denotes the mean error in the velocity dispersion (see Appendix B) and a is the bisector slope of the A 2218 and 2390 subsamples. This error in the mean luminosity evolution is given as the $\pm1\sigma$ uncertainty in Table 5. For the total sample of 96 galaxies we detect in the FJR a luminosity evolution of $0.32 \pm$

Table 5. Evolution of the Faber–Jackson relation in the Gunn r band derived for various samples. N is the number of galaxies and $\Delta\,\overline{M}_r$ indicates the mean luminosity evolution (in mag). The fourth column denotes the $\pm1\sigma$ deviation in the mean luminosity evolution and the final column $\Delta\,\langle M_r\rangle$ gives the median evolution (in mag).

Sample	N	$\Delta\,\overline{M}_r$	σ	$\Delta\,\langle M_r\rangle$
A 2218	48	0.31	0.15	0.29
A 2390	48	0.32	0.29	0.35
A 2218+A 2390	96	0.32	0.22	0.35
Low mass[a]	48	0.62	0.34	0.63
High mass	48	0.02	0.16	0.01
In[b]	48	0.26	0.20	0.24
Out[c]	48	0.35	0.20	0.40

[a]Less massive: $\log(\sigma) < 2.231$, more massive: $\log(\sigma) > 2.231$.
[b] In: only core sample $R < 458.4$ kpc,
[c]Out: only outer region sample $R > 458.4$ kpc.

0.22 mag. Similar offsets are deduced for each cluster separately. The early-type galaxies in A 2218 show an evolution of 0.31 ± 0.15 mag, whereas the E+S0 galaxies in A 2390 are brighter by 0.32 ± 0.29 mag. Both results agree with the BC96 model predictions. Dividing our sample with respect to luminosity at $M_r = -21.49$ in two groups of equal number, the difference in mean luminosity between lower- and higher-luminosity galaxies is negligible. Both subsamples have a similar slope with an insignificant slope change ($\Delta a = 0.2 \pm 0.5$).

5.2.1 Mass dependence

As the distant galaxies cover a broad range in velocity dispersions ($\log 2.02 \leqslant \sigma \leqslant 2.58$) down to 105 km s^{-1}, it is also possible to explore any evolution in the slope of the FJR. The Coma sample has a steeper slope than that of the distant clusters, with a slope difference of $\Delta a = 1.5 \pm 0.4$ (see Fig. 5). This gives some evidence for a difference between massive and less massive E+S0 galaxies. Subdividing the total sample with respect to their velocity dispersion at $\sigma <$ 170 km s^{-1} [$\log(\sigma) = 2.231$] into two subsamples of equal number, the lower-mass objects [$\log(\sigma) < 2.231$] show on average a larger evolution with $\Delta\,\overline{M}_r = 0.62 \pm 0.34$ mag. More massive galaxies [$\log(\sigma) > 2.231$] are on average brighter by $\Delta\,\overline{M}_r = 0.02 \pm 0.16$ mag. Table 5 gives a comparison between the two groups of early-type galaxies. The galaxies with lower and higher mass feature different mean velocity dispersions [$\log(\sigma) < 2.15$ and 2.34, respectively]. For this reason, a two-dimensional Kolmogorov–Smirnov (KS) test is not the appropriate statistical method for a comparison. Instead, we perform bootstrap-bisector fits to the subsamples which results in different slopes for the low and high-mass galaxies. The slope difference between the low-mass galaxies and the high-mass galaxies is $\Delta a = 2.5 \pm 1.5$, which is significant but depends on the defined selection boundaries for the local Coma reference. However, there remains the trend that less massive galaxies feature a larger luminosity offset which could be a possible hint for a faster evolution of the low-mass galaxies compared with the more massive counterparts.

5.2.2 Radial dependence

In order to investigate any possible dependence on clustercentric radius within our large data set, we have measured the distance of each galaxy from the brightest cluster galaxy and subdivided the cluster sample into two radial bins of equal size (at $R = 458.4$ kpc), so that they comprise equal numbers of galaxies. The average projected radius for galaxies in the core region is 244 kpc compared with 724 kpc for galaxies in the outer bin. Based on the relation between the virial mass of a cluster and its projected velocity dispersion, the virial radius can be derived as $R_{\rm v}$ (Mpc) $\sim 0.0035(1+z)^{-3/2}\sigma_{\rm p}\,h^{-1}$ (Girardi et al. 1998), with the projected velocity dispersion $\sigma_{\rm p}$ given in km s^{-1}. For A 2218, we adopt $\sigma_{\rm p} = 1370^{+160}_{-120}$ km s^{-1} (Le Borgne, Pello & Sanahuja 1992) and for A 2390 $R_{\rm v} = 3.156\,h^{-1}_{100}$ Mpc (Carlberg et al. 1996). For our assumed cosmology, this yields virial radii for clusters A 2218 and A2390 of $R_{\rm v} = 3.765$ Mpc (1268 arcsec) and $R_{\rm v} = 2.209$ Mpc (605 arcsec), respectively.

The mean and median evolution of the E+S0 galaxies for the central and the outer region are shown in Table 5. As the galaxies in the core and outer region feature similar mean velocity dispersions [$\log(\sigma) = 2.26$ and 2.23, respectively], the two-dimensional KS test provides a good measure of consistency. Applying the KS test results in a probability of $p = 0.46$ that the two distributions are similar. The slope for the galaxies in the core region is similar to the slope derived for the galaxies in the outskirts. Looking at the residuals from the local FJR, there is a slight trend with clustercentric radius, but it is not significantly (within $\pm1\sigma$). On average, galaxies in the outskirts of the cluster indicate a larger luminosity offset of 0.35 ± 0.20 mag than in the core region, 0.26 ± 0.20 mag. However, the offset has only a low significance and its not certain whether this gradient is real or possibly just a projection effect. Our galaxies cover a radial range out to $(R/R_{\rm v}) \sim 0.5$ (1.1 Mpc), which in the case of A 2390 is roughly the beginning of the transition region that is far from the cluster centre but still within the virial radius of the cluster. Therefore, many processes are still simultaneously at work which could account for this slight observed trend. Furthermore, our sample does not reach the outer districts of the clusters such as the complete transition or periphery zone, where a possible radial gradient with luminosity would be more apparent. We will readdress this issue in our next paper with respect to the line strength measurements for our galaxies.

5.3 Kormendy relation

Another useful probe to study the evolution is the Kormendy relation (KR; Kormendy 1977), which is the projection of the FP on the photometric plane. As this relation does not comprise galaxy kinematics, it can be studied to fainter magnitudes and therefore higher redshifts. However, the KR samples have larger scatter than in the FP and are more affected by selection biases (Ziegler et al. 1999). Nevertheless, results on the Kormendy relation should complement and endorse findings obtained with the FP. The Kormendy relation in Gunn r band for the galaxies in A 2390 and A2218 is shown in Fig. 6. The structural parameters of effective radius $R_{\rm e}$ and mean surface brightness within $R_{\rm e}$, $\langle\mu_{\rm e}\rangle$, are based on the curve of growth fits and derived using a combination of disc and bulge surface brightness models. In the upper right-hand corner we show an average error which enters the KR in the coupled form $\log(R_{\rm e}) - 0.328\,\langle\mu_{\rm e}\rangle = 0.08$, assuming a typical uncertainty of $\Delta\,\langle\mu_{\rm e}\rangle = 0.05$ and $\Delta\log(R_{\rm e}) = 0.1$. In a similar manner as for the FJR, we compute the luminosity evolution for the distant galaxies in the KR. Within our selection boundaries, a bisector fit to the Coma sample gives

$$\langle\mu_{\rm e}\rangle = 3.008\log R_{\rm e} + 18.411 \qquad (5)$$

with an observed scatter of $\sigma_{\rm KR} = 0.48$ mag in $\langle\mu_{\rm e}\rangle$. The $\pm1\sigma$ scatter of the bisector fits to the local KR is shown as solid lines in Fig. 6, whereas the bisector fits within $\pm1\sigma$ to the distant sample are indicated as the hashed area. Again, we assume a

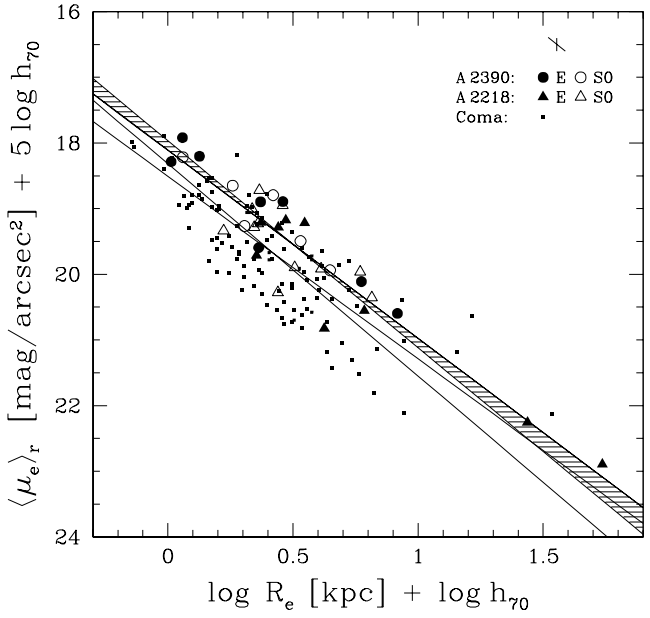

Figure 6. Kormendy relation in the Gunn r band for A 2390 and A2218, compared with the Coma sample of J99. The area bounded by solid lines indicates the $\pm 1\sigma$ errors of the bisector fits to the local KR relation. The hashed region shows the bisector fits of the distant sample within $\pm 1\sigma$. A typical error bar (mean error) is indicated in the upper right-hand corner (see the text for details).

constant slope with lookback time for determining the offsets for the distant sample from the local KR. The scatter of these offsets is $\sigma_{\rm KR} = 0.39$ mag. Comparing our galaxies within their observed magnitude range ($17.92 \leqslant \langle\mu_e\rangle \leqslant 22.89$) with the restricted Coma KR, we find a larger luminosity evolution as with the FJR. In particular, in the rest-frame Gunn r band the 34 cluster galaxies are on average brighter by 0.39 ± 0.27 mag (median value of 0.46), compared with Coma. Similar results are obtained using the de Vaucouleurs structural parameters in the KR. The E+S0 galaxies of both clusters show an offset of 0.38 ± 0.27 mag, with a median of 0.42. Note that, if $r^{1/4}$-law structural parameters are used to construct the KR, *individual* objects are differently distributed along the KR, whereas the derived *average* offsets from the local KR give similar results.

5.4 Fundamental plane

The family of early-type galaxies form a homogenous group regarding several of their properties. In a three-dimensional parameter space, defined by three observables, the effective radius R_e, effective surface brightness within R_e, $\langle\mu_e\rangle$ and velocity dispersion σ, the FP establishes a tight correlation (Djorgovski & Davis 1987; Dressler et al. 1987) in the following form:

$$\log\left(\frac{R_e}{\rm kpc}\right) = \alpha \log\left(\frac{\sigma}{\rm kms^{-1}}\right) + \beta\left(\frac{\langle\mu_e\rangle}{\rm mag\ arcsec^{-2}}\right) + \gamma. \quad (6)$$

This empirical relationship relates galaxy structure (R_e and $\langle\mu_e\rangle$) to kinematics (σ).

In general, FP studies presume that E+S0 galaxies are a homologous group, i.e. that they exhibit a similar structure. Under this assumption the total galaxy mass (including dark matter) is proportional to its virial mass $\sigma^2 R_e G^{-1}$ (Treu et al. 2001b). Elliptical galaxies do not fill the FP entirely, but rather are restricted to a certain band within it (Guzmán, Lucey & Bower 1993). Different factors account for the precise form of the FP, known as the lack of exact homology of early-type galaxies, e.g. visible in differences in the luminosity profiles or in the dynamical structure (Caon et al. 1993; Graham et al. 1996). Thanks to the small scatter of the local FP of ∼0.1 dex, the formation and evolution of E+S0 galaxies can be constrained to a good level of precision (e.g. Bender, Burstein & Faber 1992; Pahre et al. 1998).

The FP in the rest-frame Gunn r band for the distant clusters A 2218 ($z = 0.175$) and A 2390 ($z = 0.228$) is illustrated in Fig. 7. The figure also shows the FP for the local Coma samples of J99 ($z = 0.024$). All mean surface brightness magnitudes have been corrected for the dimming due to the expansion of the Universe. Errors are provided in the short edge-on FP projection (upper right-hand panel of Fig. 7), with kinematic and photometric properties on separate axes. The following results were derived. First, the FP for both individual galaxy populations and also for the combined sample show a well-defined, tight relation with a small scatter. Both intermediate redshift clusters show a similar behaviour within and along all projections of the FP. There is no evidence for an increasing scatter with redshift. Jørgensen, Franx & Kjærgaard (1996) found for a sample of 10 local clusters an rms scatter of $\sigma = 0.084$ in $\log R_e$. Our distant cluster galaxies have an rms scatter of $\sigma = 0.113$, which is not significantly higher than the local value. Secondly, only a moderate evolution of the FP and hence the stellar populations of the galaxies with redshift is seen. Assuming there is no evolution in the structure of the galaxies, i.e. at a fixed R_e and σ, the average brightening of the cluster galaxies can be determined.

The results for the FP in the rest-frame Gunn r band are presented in Table 6. We show the mean and median zero-point offsets from the local Coma FP, their 1σ scatter and the derived luminosity evolution. For the combined sample of 34 early-type cluster galaxies we deduce a ZP offset of $\Delta\gamma = 0.10 \pm 0.06$ compared with the local Coma reference, which corresponds to a modest luminosity evolution of $\Delta\,\mu_e = 0.31 \pm 0.18$ mag. Our results are consistent with the picture of simple passive evolution models (e.g. BC96). Assuming a formation redshift of $z_f = 2$ for all stars, for example, these models predict a brightening by $\Delta m_r \approx 0.20$ mag. For the individual clusters, different results are obtained. A zero-point offset of 0.16 ± 0.06 for A 2390 alone is found, meaning that the early-type galaxies in A 2390 are on average more luminous by $\Delta\mu_e = 0.49 \pm 0.18$ mag than the local Coma sample of J99. For the E+S0 in A 2218 we detect an offset of $\Delta\gamma = 0.03 \pm 0.06$, corresponding to a brightening of the stellar populations by $\Delta\,\mu_e = 0.09 \pm 0.18$ mag. This different result for the clusters may be caused by a combination of two effects: (i) a possible effect due to cosmic variance and (ii) sample selection. For example, Jørgensen et al. (1999) have analysed two different clusters (A 665 and A2218) both at a redshift of $z = 0.18$ and found a slightly different evolution of $\Delta\,\mu_e \sim 0.15$ mag. This may give evidence that not all rich clusters have the same FP zero-point offset and that cosmic variance must be accounted for. Another reason may arise from our sample selection. In the case of A 2390 particularly fainter galaxies have been selected in order to gain additional insights into the low-mass end of the FP at $z \sim 0.2$. For this reason, the A 2390 FP subsample comprises more low-luminosity galaxies than that of A 2218, which results on average in a stronger luminosity evolution for the A 2390 cluster. Table 6 gives a comparison between the two subsamples of less and more massive galaxies and between faint and bright galaxies. If we divide the total sample with regard to velocity dispersion at ∼192 km s^{-1} [corresponding to $\log(\sigma) < 2.283$] into two subsamples of different mass, we derive a stronger evolution by $\Delta\,\mu_e = 0.47 \pm 0.24$ mag for the low-mass galaxies with respect to their

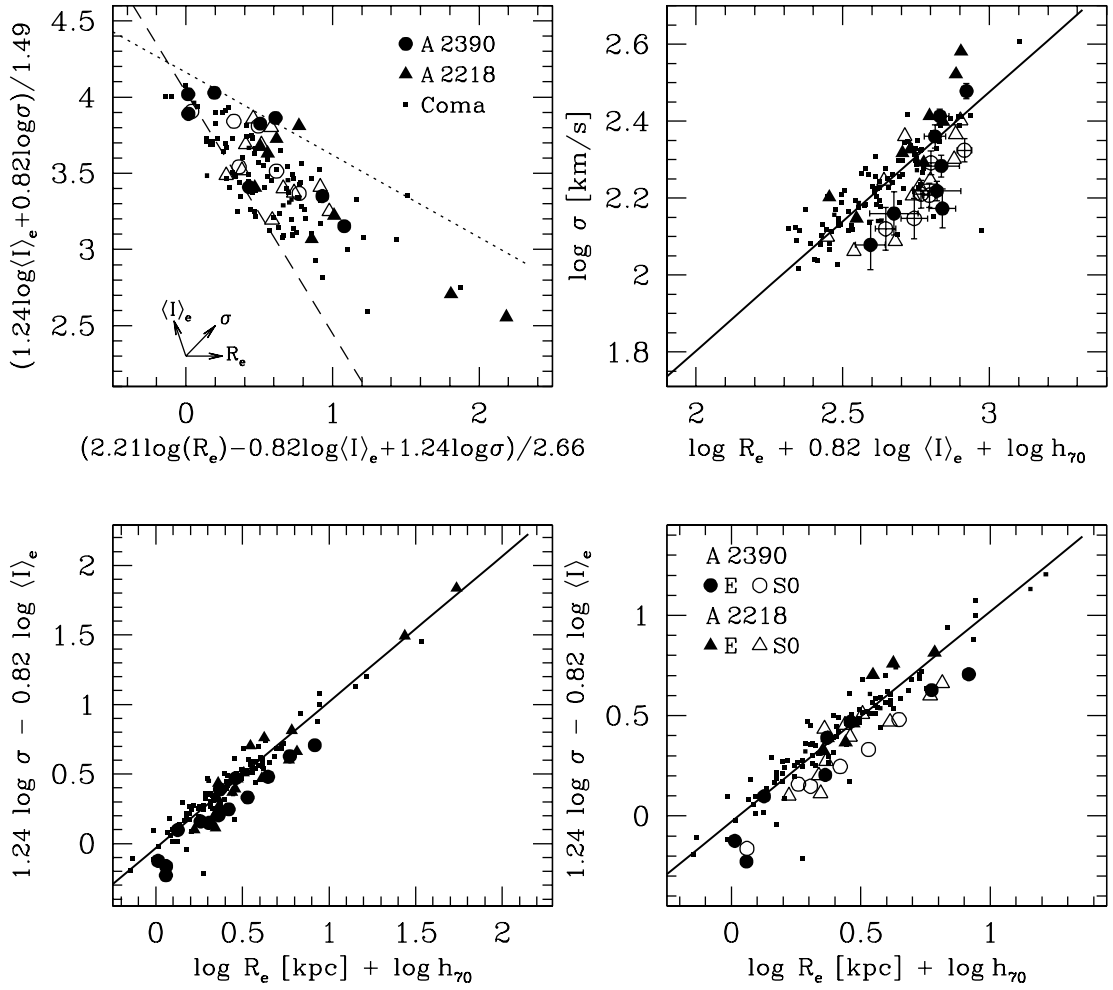

Figure 7. FP for A 2390 at $z = 0.23$ (circles) and A 2218 at $z = 0.18$ (triangles) in the rest-frame Gunn r band, compared with the Coma galaxies of J99 (small squares). Filled symbols denote ellipticals, open symbols S0 galaxies and Sa bulges. Upper panel, left: face on FP. The dotted line indicates the so-called 'exclusion zone' for nearby galaxies (Bender et al. 1992), the dashed line the luminosity limit for the completeness of the Coma sample $M_{r\,\mathrm{T}} = -20.02$ mag. Upper panel, right: FP edge-on, along the short axis. The solid line represents the bisector fit for the local Coma sample. Lower panel: edge-on FP. On the right-hand side a zoom of the edge-on FP with a separation into different morphologies is shown.

more massive counterparts, $\Delta\,\mu_{\mathrm{e}} = 0.03 \pm 0.21$. Similar results are found when we make a cut in luminosity at $M_r = -21.493$, although with a larger scatter. Looking at the thickness of the FP with respect to luminosity, we do not find an increasing scatter for the fainter galaxies within our sample. However, our subsample is too small to test the scatter of the FP in greater detail. Jørgensen et al. (1996), for example, divided their local sample with respect to luminosity into faint ($M_r > -23.16$ mag) and bright galaxies and reported a larger rms scatter for the lower-luminosity galaxies of 0.086. They argued that the larger scatter may be a result of the presence of discs or larger variations in the stellar populations of lower-luminosity galaxies. The difference between the lower- and higher-luminosity galaxies in our sample is also visible in the size distribution of the two samples (Fig. 4) and in the KR, with A 2390 containing more galaxies with small sizes and three even with $\log R_{\mathrm{e}} \leqslant 0.05$.

5.4.1 Elliptical versus lenticular galaxies

Local investigations based on the FP have not revealed significant differences in the zero-point, slope and/or scatter between elliptical and lenticular galaxies (Bender et al. 1992; Bender, Burstein & Faber 1993; Saglia et al. 1993; Jørgensen et al. 1996). Moreover, they behave very similarly to one single group of galaxies with respect to their M/L ratios and within the FP. Going to higher redshifts, differences could be more significant if recent star formation activity plays a role for S0 galaxies. However, previous studies of samples at higher redshift did not find any differences between elliptical and S0 galaxies (van Dokkum & Franx 1996; Kelson et al. 1997; van Dokkum et al. 1998). For example, within the large sample of 30 early-type galaxies in CL 1358+62 at $z = 0.33$ of Kelson et al. (2000b), the 11 ellipticals displayed identical zero-points as the 13 (non-E+A) S0 galaxies with no hint of an offset between these groups at all. Moreover, the difference in the slope of ∼14 per cent detected between the S0 and elliptical galaxies is not significant.

For the case of S0 galaxies, two main questions are still a matter of debate. How many are a priori S0 galaxies? Which and how many are the result of galaxy transformations and account for the dominant S0 population in rich clusters today? For scenarios which suggest a transformation of star-forming spiral galaxies into passive S0 systems (Dressler et al. 1997; Kodama et al. 2001), these objects can only be classified as lenticular after their morphology has been changed (∼5 Gyr). However, after this relatively long time-scale,

Table 6. Evolution of the FP in the Gunn r band as derived for various samples. N shows the number of galaxies and $\Delta\,\overline{\gamma}$ indicates the mean FP zero-point offset. In the fourth and fifth columns, the median FP zero-point evolution $\Delta\,\langle\gamma\rangle$ and the median evolution in the FP $\Delta\,\langle\mu_{\rm e}\rangle$ (in mag) are listed. The final column gives the $\pm1\sigma$ scatter of the mean offsets.

Sample	N	$\Delta\,\overline{\gamma}$	$\Delta\,\langle\gamma\rangle$	$\Delta\,\langle\mu_{\rm e}\rangle$	σ
A 2218	20	0.032	0.026	0.079	0.108
A 2390	14	0.140	0.158	0.482	0.088
A 2218+A 2390	34	0.076	0.100	0.305	0.113
E[a]	17	0.032	0.008	0.024	0.122
S0[a]	17	0.120	0.144	0.439	0.085
E (pure $r^{1/4}$)[b]	17	0.032	−0.010	−0.030	0.125
S0 (pure $r^{1/4}$)[b]	17	0.115	0.134	0.409	0.079
Low lum.[c]	17	0.085	0.100	0.305	0.114
E	8	0.070	0.074	0.226	0.127
S0	9	0.098	0.122	0.372	0.107
High lum.	17	0.068	0.093	0.284	0.114
E	9	−0.001	−0.020	−0.061	0.114
S0	8	0.145	0.168	0.512	0.045
Low mass[d]	17	0.129	0.153	0.466	0.106
E	6	0.114	0.158	0.482	0.150
S0	11	0.138	0.153	0.466	0.080
High mass	17	0.023	0.010	0.030	0.095
E	11	−0.012	−0.015	−0.046	0.081
S0	6	0.087	0.100	0.305	0.091

[a] Based on $r^{1/4}$+exp. disc surface brightness profiles.
[b] $r^{1/4}$ surface brightness profile only.
[c] Lower luminosity: $M_r > -21.493$, higher luminosity: $M_r < -21.493$.
[d] Less massive: $\log(\sigma) < 2.283$, more massive: $\log(\sigma) > 2.283$.

their star formation could have already ceased, which would make these galaxies hard to detect. E+A galaxies could represent galaxies in an intermediate state of such a transformation where harassment has just stopped but SF is still present due the result of a starburst which ended within the last 1.5–2 Gyr (Barger et al. 1996). Recently, Yang et al. (2004) performed a study of E+A galaxies in the local Universe and argued that these objects only show an offset in their surface brightnesses but not in their total magnitudes. Such galaxies would be invisible in the FJR but could be revealed within the FP.

Fig. 8 illustrates the edge-on view of the FP for 34 E+S0 galaxies of the clusters A 2218 and A2390 in the rest-frame Gunn r band. The FP constructed for the distant clusters at intermediate redshift is compared with the FP for the local Coma sample of J99, indicated by the bisector fit. Our combined sample represents a comparable data set to the study by Kelson et al. (2000b) and hence one of the most extensive investigations of early-type galaxies in clusters at $z \sim 0.2$. Fig. 8 has been split in order to visualize the small variations if different luminosity profile fits are used for deriving structural parameters. The left-hand figure displays the FP constructed using a combination of an $r^{1/4}$-law+exponential disc profile and the right-hand figure is based on pure $r^{1/4}$-law fits. The variations in the structural parameters only affect the galaxies moving along the edge-on projection of the FP, thereby maintaining the tightness of the plane. As shown by Graham & Colless (1997), both the $r^{1/4}$ FP and $r^{1/n}$ FP have the same scatter and slope within their errors. A second comparison is given by the FP parameter $R_{\rm e}\,I_{\rm e}^{0.8}$ in Tables 2 and 3 (column 9). In general, the agreement is good for both elliptical and S0 galaxies.

We will now consider in more detail possible differences between elliptical and lenticular galaxies. As a local reference we adopt the Coma FP coefficients of J99 in the Gunn r band. The choice of the fitting technique, the selection criteria and the measurement errors that are correlated can lead to systematic uncertainties in the FP coefficients, $\sim\pm0.1$ dex (Jørgensen et al. 1996; Kelson et al. 2000b). A morphological analysis of the *HST* images revealed that our A 2390 subsample splits nearly equally into elliptical (eight) and lenticular (S0) galaxies (six). Both ellipticals and lenticular galaxies are uniformly distributed along the surface of the FP. An edge-on projection can therefore be taken for a robust comparison of their stellar populations. Table 6 lists the derived evolution for the E and S0 galaxies. Fixing the slope of the local Coma reference, the zero-point offset for the S0 galaxies in our sample is:

$$\Delta\gamma_{\rm S0,z=0.2} = 0.14 \pm 0.06. \quad (7)$$

This zero-point offset for lenticular galaxies corresponds to an evolution of $\Delta\,\mu_{\rm e} = 0.44 \pm 0.18$ mag with respect to the local counterparts. On the other hand, the ZP offset for the ellipticals yields:

$$\Delta\gamma_{\rm E,z=0.2} = 0.01 \pm 0.07. \quad (8)$$

Restricting our sample to the elliptical galaxies we derive a negligible zero-point deviation with respect to the local FP, which corresponds to an insignificant luminosity evolution of $\Delta\,\mu_{\rm e} = 0.02 \pm 0.21$ mag which is within their 1σ scatter. For the combined sample of 34 E+S0 cluster galaxies we derive a median offset of:

$$\Delta\gamma_{\rm E+S0,z=0.2} = 0.10 \pm 0.06, \quad (9)$$

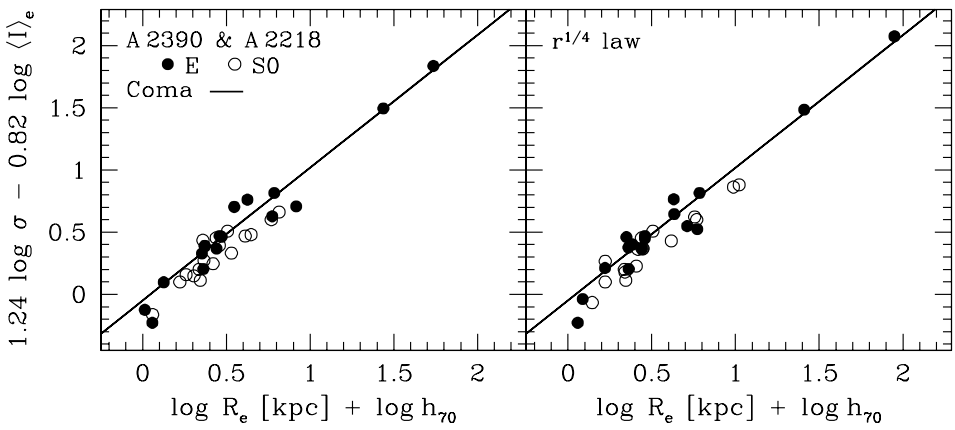

Figure 8. Edge-on view of the FP for A 2390 and A2218 in rest-frame Gunn r. The distant FP is compared with the FP of the local Coma sample of J99, indicated by the 100 iteration bootstrap bisector fit (thick solid line). Left: FP constructed using a combination of an $r^{1/4}$ and exponential disc profile. Right: similar to the left-hand plot except that $r^{1/4}$-law parameters were used.

which corresponds to a brightening of the stellar populations by 0.31 ± 0.18 mag. On average, the lenticular galaxies in our sample show a larger luminosity evolution than the ellipticals. In both interpretations of Fig. 8 the S0 galaxies are predominantly located below the ellipticals and may indicate a different evolutionary trend between the stellar populations of elliptical and S0 galaxies. Dividing our sample with respect to velocity dispersion into a low-mass [$\log(\sigma) < 2.283$] and a high-mass subsample [$\log(\sigma) > 2.283$], we find a different evolution. The lower-mass galaxies are on average, with 0.47 ± 0.24 mag, more luminous than their more massive counterparts with 0.03 ± 0.21 mag at $z \sim 0.2$. This is also seen for the different subgroups of elliptical and S0 galaxies, but with less significance (see Table 6).

In conclusion, we derive for the whole sample of 34 E+S0 galaxies only a moderate amount of luminosity evolution. From these results and the previous findings of the FJR and KR, we conclude that at a lookback time of $\sim$2.8 Gyr most early-type galaxies of A 2218 and A2390 consist of an old stellar population with the bulk of the stars formed at a high formation redshift of approximately $z_f \geqslant 4$.

5.5 The M/L ratio as a diagnostic for stellar populations

Under the assumption of homology of the early-type galaxies, the existence of the tight FP implies that the global mass-to-light (M/L) ratio of early-type galaxies is related to the mass M of an object in the following form (Faber et al. 1987):

$$M/L_r \propto \sigma^{0.49} R_e^{0.22} \propto M^{0.24} R_e^{-0.02}. \quad (10)$$

The small scatter of ± 0.10 dex within the FP implies a scatter of only 23 per cent in their M/L ratios.

The evolution of the FP can be characterized in terms of its zero-point. In turn, the zero-point of the FP is related to the mean M/L ratio. Thus, if the FP zero-point for a sample of early-type galaxies changes as a function of redshift z, this implies an evolution of the mean M/L ratio and hence an evolution in the luminosity-weighted stellar population properties of the galaxies under consideration.

For the present-day zero-point of the FP we performed a bootstrap bisector fit to the early-type Coma galaxies in the rest-frame Gunn r band. This yields a slope of 1.048 ± 0.038 and a zero-point of 0.412 ± 0.010. The early-type galaxies of A 2390 show a small shift with respect to the Coma galaxies (see Fig. 7). As the velocity dispersions and effective radii of the galaxies in A 2390 span similar ranges such as their local counterparts (apart from the Coma cD galaxies with $R_e \gtrsim 30$ kpc) and the surface brightnesses are slightly increased with respect to the local sample, at least some of the shift in the M/L ratio is due to luminosity evolution. However, when deriving an exact amount of luminosity evolution, one has to be careful as additional combined effects also contribute to the total derived luminosity offset. Some studies found different FP slopes at intermediate redshift compared with the local slope, but they suffer from low number statistics (van Dokkum & Franx 1996; Kelson et al. 1997; van Dokkum et al. 1998). However, more recent investigations based on larger samples reported similarly only a modest change in the FP slope (Kelson et al. 2000b; Treu et al. 2001b; Z01). Thus, the lack of a strong slope change gives evidence against the hypothesis of the FP being solely an age–mass relation. The FP is mainly a relation between the M/L ratio and the galaxy mass M. Therefore, when comparing small samples with significantly different ranges in galaxy mass, an offset in the M/L ratio can depend heavily on the adopted FP slope. The M/L offset will be a combination of three items: (i) the difference in the slope of the FP; (ii) the mean mass range of the sample; and (iii) the 'true' offset. By reducing the differences in the mass distribution, the M/L results become insensitive to the adopted slope of the FP and any derived evolution for the distant galaxies is valid for a given range of galaxy masses (Kelson et al. 2000b). For this reason, we have restricted the local Coma sample to a similar mass function as for the galaxies in A 2218 and A2390.

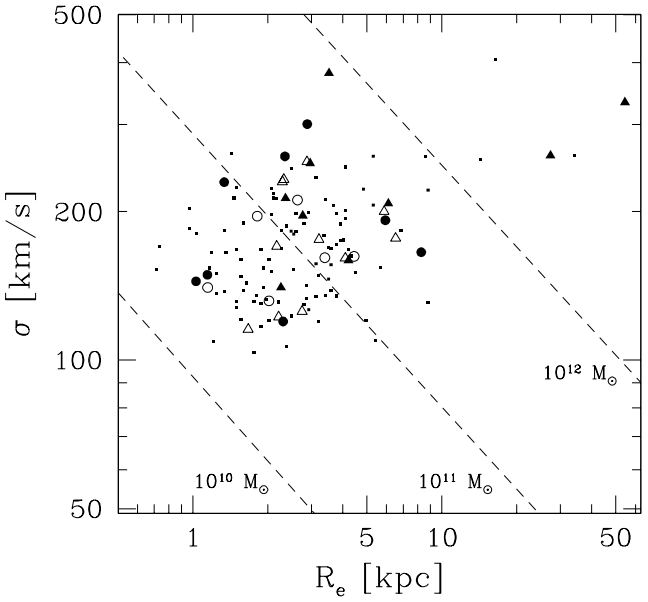

Figure 9. The $\log\sigma$–$\log R_e$ plane for the A 2390 and A2218 early-type galaxies, compared with the Coma galaxies of J99. Symbol notations as in Fig. 7. Dashed lines indicate contours of constant mass $5G^{-1}\sigma^2 R_e = 10^{10}$, 10^{11} and $10^{12}\,M_\odot$ (Bender et al. 1992). The early-type galaxy masses of A 2390 and A2218 at $z \sim 0.2$ are distributed similarly to the early-type Coma sample.

A comparison of the mass distributions of the distant early-type galaxies of A 2390 and A2218 with the local Coma galaxies within the $\log\sigma$–$\log R_e$ plane is shown in Fig. 9. Regions of constant mass, ranging from 10^{12} and 10^{11} down to $10^{10}\,M_\odot$, derived with the relation $M = 5\sigma^2 R_e/G$ in units of $M_\odot$ (Bender et al. 1992) where G is the gravitational constant, are indicated as dashed lines. Both samples exhibit similar ranges in mass (σ) and size (R_e), ensuring that a possible M/L evolution will not be driven mainly by any differences between the galaxy mass ranges of the samples.

Adopting a constant slope with redshift, the median zero-point offset for the combined sample of 34 E+S0 cluster galaxies yielded $\Delta\gamma_{E+S0,z=0.2} = 0.10 \pm 0.02$ (where the error corresponds to the uncertainty as derived via the bootstrap method). Alternatively, using a variable slope in the FP for the distant cluster sample, we find negligible changes in the FP parameters α and β compared with the locally defined parameters by the Coma data. In particular, a bootstrap bisector fit to all 34 E+S0 galaxies gives a slightly steeper slope of 1.152 ± 0.047 and a zero-point offset of 0.024 ± 0.018, with a 1σ confidence level for a slope change. This comparison and the results based on the M/L ratios may give some evidence for a mass-dependent evolution which is stronger for low-mass galaxies.

Fig. 10 shows the observed mass-to-light M/L ratio of the distant clusters A 2218 and A2390 as a function of velocity dispersion σ (left) and versus mass M (right). We limited the Coma sample to galaxies with $\log\sigma > 2.02$ (indicated by the vertical dotted lines in Fig. 10) in order to match the area of parameter space covered

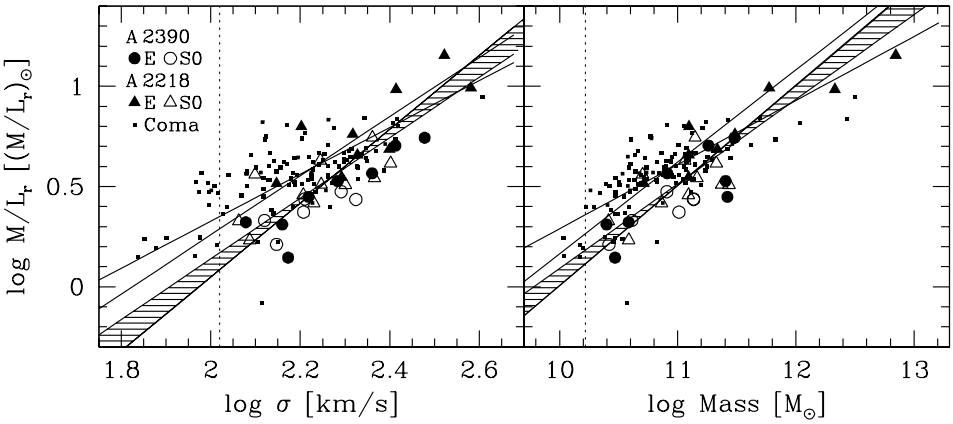

Figure 10. The M/L ratio in Gunn r band for A 2390 and A2218 as a function of velocity dispersion σ (left) and as a function of mass in solar units (right). Symbol notation as in Fig. 7. Solid lines show the 100 iteration bootstrap bisector fits to the local Coma sample of J99 within selection boundaries of the distant samples (1σ errors). The hashed area denotes the bisector fits within 1σ errors to the combined distant sample of A 2390 and A2218.

by the distant galaxies of A 2390 and A2218. An analysis based on bootstrap bisector fits to $M/L = a\sigma^m$ revealed different M/L slopes for the distant (hashed area) and the local (solid lines) samples. The slope difference between A 2218 and Coma is $\Delta m_{\rm A2218} = 0.27 \pm 0.17$ and the offset in the zero-point is $\Delta a_{\rm A2218} = 0.040 \pm 0.027$. For A 2390 we detect $\Delta m_{\rm A2390} = 0.11 \pm 0.21$ and $\Delta a_{\rm A2390} = 0.157 \pm 0.019$. The combined sample of distant clusters has a slope difference of $\Delta m_{z=0.2} = 0.36 \pm 0.17$ and $\Delta a_{z=0.2} = 0.036 \pm 0.024$. We measure with a 2σ confidence different slopes for both the intermediate clusters and the Coma cluster (Coma slope value of $m = 0.59 \pm 0.15$). However, we detect a systematic zero-point offset of the distant M/L relation of $\Delta a_{z=0.2} = 0.04 \pm 0.02$, which is not in agreement with the proposed change due to passive evolution with $z_{\rm f} = 2$ ($\Delta a = 0.12$). Ellipticals and S0 galaxies seem to have different M/L slopes changes, with a steeper slope for the elliptical galaxies. Ellipticals: $\Delta m_{\rm E} = 0.54 \pm 0.30$ and $\Delta a_{\rm E} = 0.041 \pm 0.037$; S0s: $\Delta m_{\rm S0} = 0.06 \pm 0.23$ and $\Delta a_{\rm S0} = 0.141 \pm 0.026$.

The M/L ratios as a function of mass M are shown in the right-hand plot of Fig. 10. In a similar manner as for the velocity dispersions, the two samples are analysed in terms of bootstrap bisector fits. For the Coma cluster alone we find $M/L \propto M^{0.59\pm0.07}$. With respect to Coma, the slope difference for A 2218 is $\Delta m_{\rm A2218} = 0.025 \pm 0.060$ with a zero-point offset of $\Delta a_{\rm A2218} = 0.048 \pm 0.029$. For A 2390 a similar slope change is found, $\Delta m_{\rm A2390} = 0.057 \pm 0.063$, but with a larger offset of $\Delta a_{\rm A2390} = 0.165 \pm 0.028$. The two distant clusters as a whole have $\Delta m_{z=0.2} = 0.071 \pm 0.039$ and $\Delta a_{z=0.2} = 0.037 \pm 0.021$. Dividing the sample into elliptical and S0 galaxies gives no significant slope changes, for Es: $\Delta m_{\rm E} = 0.049 \pm 0.056$ and for S0s: $\Delta m_{\rm S0} = 0.087 \pm 0.089$. However, the S0s exhibit a larger offset in the zero-point of $\Delta a_{\rm S0} = 0.138 \pm 0.030$, compared with the ellipticals $\Delta a_{\rm E} = 0.050 \pm 0.034$.

The correction of the so-called 'progenitor bias' (van Dokkum & Franx 2001) for our sample has an insignificant influence on the results in the FP and on the M/L ratios (at $z = 0.2$ the evolution in the M/L ratio is underestimated by $\Delta\ln\langle M/L_B\rangle \approx 0.2\,z \approx 0.04$). Therefore, we have neglected it. This effect comes into play at a redshift of approximately $z \gtrsim 0.4$ and has a dramatic effect at high redshifts of approximately $z \geqslant 0.8$.

6 CONCLUSIONS

We have investigated the evolution for a total of 96 early-type galaxies in two massive, X-ray luminous clusters of galaxies, Abell 2218 ($z = 0.175$) and Abell 2390 ($z = 0.228$). The data of Abell 2218 was already described in Z01, whereas new kinematics and structural parameters of 48 early-type galaxies in the cluster Abell 2390 are presented. These combined data sets represent one of the largest samples at a redshift of $z \sim 0.2$, ideally suited to studying the evolution of early-type cluster galaxies. For the whole sample we have constructed the Faber–Jackson relation (FJR) and for a subsample of 34 early-type galaxies, we have explored the evolution of the FP and the KR. Our main results are as follows.

(i) In the FJR we find a modest luminosity evolution of the 96 early-type galaxies with respect to the local reference. For the total sample the average offset from the local FJR in the Gunn r band is $\Delta\,\overline{M}_r = 0.32 \pm 0.22$ mag. Similar findings are obtained if we restrict the sample to the individual clusters. A 2390 has a mean brightening of 0.32 ± 0.29 mag, A 2218 shows an evolution of 0.31 ± 0.15 mag. Both results agree with the BC96 model predictions for a passive evolution of the stellar populations assuming a formation redshift of $z_{\rm f} = 2$.

(ii) Splitting the total sample of the FJR with respect to velocity dispersion, less massive galaxies ($\sigma < 170$ km s^{-1}) show a trend for a larger evolution with $\Delta\,\overline{M}_r = 0.62 \pm 0.34$ mag compared with their more massive counterparts $\Delta\,\overline{M}_r = 0.02 \pm 0.16$ mag. There is little evidence for a small gradient with clustercentric radius with slightly brighter luminosities for galaxies in the outer regions.

(iii) The 34 early-type cluster galaxies obey a tight fundamental plane relation with a small scatter of 0.11 dex at $z \sim 0.2$. We find no evidence for an increasing scatter with redshift. For the combined cluster samples we detect a mild luminosity evolution with a zero-point offset of $\Delta\gamma_{z=0.2} = 0.10 \pm 0.06$ with respect to the local Coma FP relation. The cluster A 2390 alone indicates a larger evolution of $\Delta\gamma_{\rm A\,2390} = 0.16 \pm 0.06$. However, this is due to a larger number of low-mass galaxies in the case of A 2390. For A2218 we derive $\Delta\gamma_{\rm A\,2218} = 0.03 \pm 0.06$.

(iv) Subdividing our sample in terms of morphology yielded two subsamples of elliptical (E) and lenticular (S0) galaxies that are equal in size. Ellipticals and S0 galaxies are uniformly distributed along the FP (Fig. 7), with a similar scatter of 0.1 dex. The subsamples show a median zero-point offset from the local reference of $\Delta\gamma_{\rm E} = 0.01 \pm 0.07$ and $\Delta\gamma_{\rm S0} = 0.14 \pm 0.06$, respectively. We find little evidence for differences between elliptical and S0 galaxies within our sample. Lenticular galaxies alone induce on

average a larger evolution, thereby residing in a zone in the FP below the ellipticals.

(v) An analysis of the M/L ratios for the distant galaxies revealed a steeper slope than that of the local counterparts. This effect is weaker than that derived by Jørgensen et al. (1999) for a composite of five intermediate redshift clusters. The subsamples of ellipticals and S0s appear to have different M/L slopes, with a trend for a steeper slope for the elliptical galaxies (Fig. 10). The M/L ratios as a function of mass M indicate no differences in the slopes between elliptical and lenticular galaxies. However, the S0 galaxies feature a larger zero-point offset.

Our results are in good agreement with previous observational studies on rich clusters at intermediate and higher redshifts (Jørgensen et al. 1999; Kelson et al. 2000b; Wuyts et al. 2004). These investigations suggest that the mild luminosity evolution derived for their galaxies is consistent with stellar population models of passive evolution. Assuming a formation redshift of $z_{\rm f} = 2$, the BC96 models predict in the Gunn r band a brightening by 0.21 mag at $z = 0.2$. This is in good agreement with the findings we derive for the FJR and FP. For the cluster A 2390 alone, we detect a larger evolution in the FP and KR. This may be the result of a combination of both cosmic variance and of a larger number of low-luminosity galaxies. Our results are consistent with the monolithic collapse scenario and a passive evolution of the stellar populations.

In a forthcoming paper, we will explore the line strengths for our early-type galaxies in order to analyse the stellar populations of the E+S0 cluster galaxies with respect to age, metallicity and abundance ratios. Results of the line indices will be compared with stellar population models and will reveal if there are different subpopulations between elliptical and lenticular galaxies with respect to their age or metallicity or a combination of both properties.

ACKNOWLEDGMENTS

This work is based on observations collected at the Centro Astronómico Hispano Alemán (CAHA) at Calar Alto, operated by the Max-Planck-Institut für Astronomie, Heidelberg, jointly with the Spanish National Commission for Astronomy. We thank the anonymous referee for constructive criticism that improved the clarity of this manuscript. We would like to thank Professor K. J. Fricke for encouragement and support and are grateful to Drs A. Böhm and A. W. Graham for stimulating discussions and valuable comments. We thank the Calar Alto staff for efficient observational support. AF and BLZ acknowledge financial support by the Volkswagen Foundation (I/76 520) and the Deutsche Forschungsgemeinschaft (ZI 663/1-1, ZI 663/2-1). IRS acknowledges support from the Royal Society and the Leverhulme Trust.

This work is based on observations with the Hale Telescope at Palomar Observatory, which is owned and operated by the California Institute of Technology. This research has made use of the NASA/IPAC Extragalactic Data base (NED), which is operated by the Jet Propulsion Laboratory, California Institute of Technology, under contract with the National Aeronautics and Space Administration.

REFERENCES

Barger A. J., Aragon-Salamanca A., Ellis R. S., Couch W. J., Smail I., Sharples R. M., 1996, MNRAS, 279, 1
Barnes J. E., Hernquist L., 1992, ARA&A, 30, 705
Baugh C. M., Cole S., Frenk C. S., 1996, MNRAS, 283, 1361
Bender R., 1988, A&A, 193, L7
Bender R., 1990, A&A, 229, 441
Bender R., Möllenhoff C., 1987, A&A, 177, 71
Bender R., Döbereiner S., Möllenhoff C., 1988, A&AS, 74, 385
Bender R., Burstein D., Faber S. M., 1992, ApJ, 399, 462
Bender R., Burstein D., Faber S. M., 1993, ApJ, 411, 153
Bernardi M., Renzini A., da Costa L. N., Wegner G., Alonso M. V., Pellegrini P. S., Rité, C., Willmer C. N. A., 1998, ApJ, 508, L143
Bernardi M. et al., 2003, AJ, 125, 1866
Bertin E., Arnouts S., 1996, A&AS, 117, 393
Bruzual G. A., Charlot S., 1993, ApJ, 405, 538
Caon N., Capaccioli M., D'Onofrio M., 1993, MNRAS, 265, 1013
Carlberg R. G., Yee H. K. C., Ellingson E., Abraham R., Gravel P., Morris S., Pritchet C. J., 1996, ApJ, 462, 32
Cole S., Lacey C. G., Baugh C. M., Frenk C. S., 2000, MNRAS, 319, 168
de Carvalho R. R., Djorgovski S., 1992, ApJ, 389, L49
Djorgovski S., Davis M., 1987, ApJ, 313, 59
Dressler A., Lynden-Bell D., Burstein D., Davies R. L., Faber S. M., Terlevich R., Wegner G., 1987, ApJ, 313, 42
Dressler A. et al., 1997, ApJ, 490, 577
Ellis R. S., Smail I., Dressler A., Couch W. J., Oemler A. J., Butcher H., Sharples R. M., 1997, ApJ, 483, 582
Faber S. M., Jackson R. E., 1976, ApJ, 204, 668
Faber S. M., Dressler A., Davies R. L., Burstein D., Lynden-Bell D., Terlevich R., Wegner G., 1987, Nearly Normal Galaxies. Springer, New York, p. 175
Faber S. M., Wegner G., Burstein D., Davies R. L., Dressler A., Lynden-Bell D., Terlevich R. J., 1989, ApJS, 69, 763
Fritz A., Ziegler B. L., Bower R. G., Smail I., Davies R. L., 2004, in Mulchaey J. S., Dressler A., Oemler A., eds, Clusters of Galaxies: Probes of Cosmological Structure and Galaxy Evolution. Carnegie Observatories, Pasadena, http://www.ociw.edu/ociw/symposia/series/symposium3/proceedings.html
Fukugita M., Shimasaku K., Ichikawa T., 1995, PASP, 107, 945
Girardi M., Giuricin G., Mardirossian F., Mezzetti M., Boschin W., 1998, ApJ, 505, 74
Graham A., Colless M., 1997, MNRAS, 287, 221
Graham A., Lauer T. R., Colless M., Postman M., 1996, ApJ, 465, 534
Guzmán R., Lucey J. R., Bower R. G., 1993, MNRAS, 265, 731
Hill R. J. et al., 1998, ApJ, 496, 648
Holtzman J. A., Burrows C. J., Casertano S., Hester J. J., Trauger J. T., Watson A. M., Worthey G., 1995, PASP, 107, 1065
Horne K., 1986, PASP, 98, 609
James P. A., Mobasher B., 1999, MNRAS, 306, 199
Jørgensen I., 1999, MNRAS, 306, 607 (J99)
Jørgensen I., Franx M., Kjærgaard P., 1995, MNRAS, 273, 1097 (J99)
Jørgensen I., Franx M., Hjorth J., van Dokkum P. G., 1999, MNRAS, 308, 833
Jørgensen I., Franx M., Kjærgaard P., 1996, MNRAS, 280, 167
Kauffmann G., Charlot S., 1998, MNRAS, 294, 705
Kelson D. D., van Dokkum P. G., Franx M., Illingworth G. D., Fabricant D., 1997, ApJ, 478, L13
Kelson D. D., Illingworth G. D., van Dokkum P. G., Franx M., 2000a, ApJ, 531, 137
Kelson D. D., Illingworth G. D., van Dokkum P. G., Franx M., 2000b, ApJ, 531, 184
Kinney A. L., Calzetti D., Bohlin R. C., McQuade K., Storchi-Bergmann T., Schmitt H. R., 1996, ApJ, 467, 38
Kodama T., Smail I., Nakata F., Okamura S., Bower R. G., 2001, ApJ, 562, L9
Kormendy J., 1977, ApJ, 218, 333
Kormendy J., Bender R., 1996, ApJ, 464, L119
Kuntschner H., Smith R. J., Colless M., Davies R. L., Kaldare R., Vazdekis A., 2002, MNRAS, 337, 172
La Barbera F., Busarello G., Merluzzi P., Massarotti M., Capaccioli M., 2002, ApJ, 571, 790
Larson R. B., 1975, MNRAS, 173, 671
Le Borgne J. F., Mathez G., Mellier Y., Pello R., Sanahuja B., Soucail G., 1991, A&AS, 88, 133
Le Borgne J. F., Pello R., Sanahuja B., 1992, A&AS, 95, 87

Mehlert D., Thomas D., Saglia R. P., Bender R., Wegner G., 2003, A&A, 407, 423
Menanteau F., Abraham R. G., Ellis R. S., 2001, MNRAS, 322, 1
Möller C. S., Fritze-v.Alvensleben U., Fricke K. J., Calzetti D., 2001, Ap&SS, 276, 799
Moore B., Katz N., Lake G., Dressler A., Oemler A., 1996, Nat, 379, 613
Naab T., Burkert A., 2003, ApJ, 597, 893
Naab T., Burkert A., Hernquist L., 1999, ApJ, 523, L133
Pahre M. A., Djorgovski S. G., de Carvalho R. R., 1998, AJ, 116, 1591
Poggianti B. M., Smail I., Dressler A., Couch W. J., Barger A., Butcher H., Ellis R. S., Oemler A., Jr, 1999, ApJ, 518, 576
Rusin D. et al., 2003, ApJ, 587, 143
Saglia R. P., Bender R., Dressler A., 1993, A&A, 279, 75
Saglia R. P., Bertschinger E., Baggley G., Burstein D., Colless M., Davies R. L., McMahan R. K., Jr, Wegner G., 1997a, ApJS, 109, 79
Saglia R. P., Burstein D., Baggley G., Davies R. L., Bertschinger E., Colless M., McMahan R. K., Jr, Wegner G., 1997b, MNRAS, 292, 499
Sánchez-Blázquez P., Gorgas J., Cardiel N., Cenarro J., González J. J., 2003, ApJ, 590, L91
Schade D. et al., 1999, ApJ, 525, 31
Schlegel D. J., Finkbeiner D. P., Davis M., 1998, ApJ, 500, 525
Simard L. et al., 2002, ApJS, 142, 1
Smail I., Edge A. C., Ellis R. S., Blandford R. D., 1998, MNRAS, 293, 124
Smail I., Kuntschner H., Kodama T., Smith G. P., Packham C., Fruchter A. S., Hook R. N., 2001, MNRAS, 323, 839
Stanford S. A., Eisenhardt P. R., Dickinson M. E., 1998, ApJ, 492, 461
Thuan T. X., Gunn J. E., 1976, PASP, 88, 543
Toomre A., 1977, in Tinsley B. T., Larson R. B., eds, The Evolution of Galaxies and Stellar Populations. Yale Univ. Press, New Haven, p. 401
Tran K. H., Simard L., Illingworth G., Franx M., 2003, ApJ, 590, 238
Treu T., Stiavelli M., Møller P., Casertano S., Bertin G., 2001a, MNRAS, 326, 221
Treu T., Stiavelli M., Bertin G., Casertano S., Møller P., 2001b, MNRAS, 326, 237
Treu T., Stiavelli M., Casertano S., Møller P., Bertin G., 2002, ApJ, 564, L13
Treu T., Ellis R. S., Kneib J.-P., Dressler A., Smail I., Czoske O., Oemler A., Natarajan P., 2003, ApJ, 591, 53
van Dokkum P. G., Franx M., 1996, MNRAS, 281, 985
van Dokkum P. G., Franx M., 2001, ApJ, 553, 90
van Dokkum P. G., Franx M., Kelson D. D., Illingworth G. D., 1998, ApJ, 504, L17
van Dokkum P. G., Franx M., Fabricant D., Illingworth G. D., Kelson D. D., 2000, ApJ, 541, 95
van Dokkum P. G., Franx M., Kelson D. D., Illingworth G. D., 2001, ApJ, 553, L39
Wuyts S., van Dokkum P. G., Kelson D. D., Franx M., Illingworth G. D., 2004, ApJ, 605, 677
Yang Y., Zabludoff A. I., Zaritsky D., Lauer T. R., Mihos J. C., 2004, ApJ, 607, 258
Yee H. K. C., Ellingson E., Abraham R. G., Gravel P., Carlberg R. G., Smecker-Hane T. A., Schade D., Rigler M., 1996, ApJS, 102, 289
Ziegler B. L., Bender R., 1997, MNRAS, 291, 527
Ziegler B. L., Saglia R. P., Bender R., Belloni P., Greggio L., Seitz S., 1999, A&A, 346, 13
Ziegler B. L., Bower R. G., Smail I., Davies R. L., Lee D., 2001, MNRAS, 325, 1571 (Z01)

APPENDIX A: PROPERTIES OF THE *HST* SUBSAMPLE

Surface brightness profiles of those galaxies situated within the *HST* field of Abell 2390 with available spectroscopic information are shown in Fig. A1. For the surface brightnesses a correction for galactic extinction was applied. In most cases the observed profile is best fitted by a combination of a bulge (de Vaucouleurs law) and a disc component (exponential law). Values for the total magnitude $I_{\rm tot}$, the surface brightness of the disc $\mu_{\rm d,0}$, the effective radius $R_{\rm e}$ and the effective radius of the bulge $R_{\rm e,b}$, and the disc-to-bulge ratio D/B are listed. The arrow in each diagram indicates the position of the effective radius $R_{\rm e}$. Typical residuals $\Delta\mu_I$ between the observed profile and the modelled fit are of the order of ±0.10 mag at $R^{1/4} \approx 1.3$ arcsec. Note that the disc fit indicated in Fig. A1 represents the disc component of the combined best fit for the corresponding galaxies.

The single galaxy which could not be fitted (no 2933) does not reside close to the edge of the WF4 chip but is a late-type spiral galaxy (Sbc) with clear signs of spiral pattern. Thumbnail images of the cluster members are given in Fig. A2. Objects were morphologically classified in two independent ways, based on visual inspection and also the fitting routine output. A visual classification was obtained by two of us, AF and IS separately, resulting in very similar morphologies. The findings from the luminosity profile fitting provided a consistency check, which resulted in the same classification scheme except for two objects [no 2180: E (visual), S0 (fit) and no 2763: S0/Sa (visual), E (fit)]. Objects which are best described with an $r^{1/4}$ law are classified as an elliptical (E); those galaxies for which an additional exponential component yielded a slightly improved fit (without a dramatic change in structural properties) are classified as E/S0; S0 galaxies are best approximated by a combination of an $r^{1/4}$ law plus an exponential profile.

Remarks on special features on individual *HST* objects of Abell 2390 are listed in Table A1. The first column shows the galaxy ID, the second indicates the morphology of the objects. In the third column, additional information concerning special features regarding the galaxy is given.

APPENDIX B: PHOTOMETRIC PROPERTIES OF CLUSTER GALAXIES

In this section we present the photometric parameters derived from the ground-based *U*-, *B*- and *I*-band Hale imaging of the cluster Abell 2390. Table B1 shows the photometric properties of the cluster galaxies. The galaxy ID can be found in the finding chart (Fig. 1), $I_{\rm tot}$ is the total magnitude derived from the Hale images (BEST_MAG of SEXTRACTOR), $U_{\rm ap}$, $B_{\rm ap}$, and $I_{\rm ap}$ are magnitudes within a circular aperture of 3.0-arcsec diameter measured in a seeing-matched *UBI* image. None of the given magnitudes is corrected for extinction. M_r denotes the absolute rest-frame Gunn *r*-band magnitude. The velocity dispersions of the galaxies σ (in km s^{-1}) are not aperture-corrected. Column v denotes the heliocentric radial velocity (in km s^{-1}) and its error. The galaxy with ID no 3824 is presumably an E+A candidate as its spectra features strong Hβ and Hγ Balmer lines. On the ground-based images a disc is clearly visible but no further signs of spiral structure. Object no 3038 is not included, because it is a foreground galaxy at redshift of $z = 0.1798$.

For the analysis we have also excluded Sbc galaxy no 2933 and two other objects (nos 1507 and 1639) because they are all background galaxies. Their spectra suffer from a low S/N ratio and as their *G* band is affected by strong sky-lines and the Mg feature falls into the telluric *B* band no reliable velocity dispersions could be derived. The properties of these galaxies and foreground galaxy no 3038 are shown in Table B2. During the observations of our target galaxies four other galaxies fell into the slits by coincidence (nos 2222, 5552, 5553 and 6666). However, apart from object no 6666, their spectra are too faint (S/N $\lesssim$12) to determine accurate velocity dispersions. Thus, they were rejected from the final sample. For galaxy no 6666, we derived the absolute Gunn *r*-band magnitude using our *HST* photometry and included it in our data set.

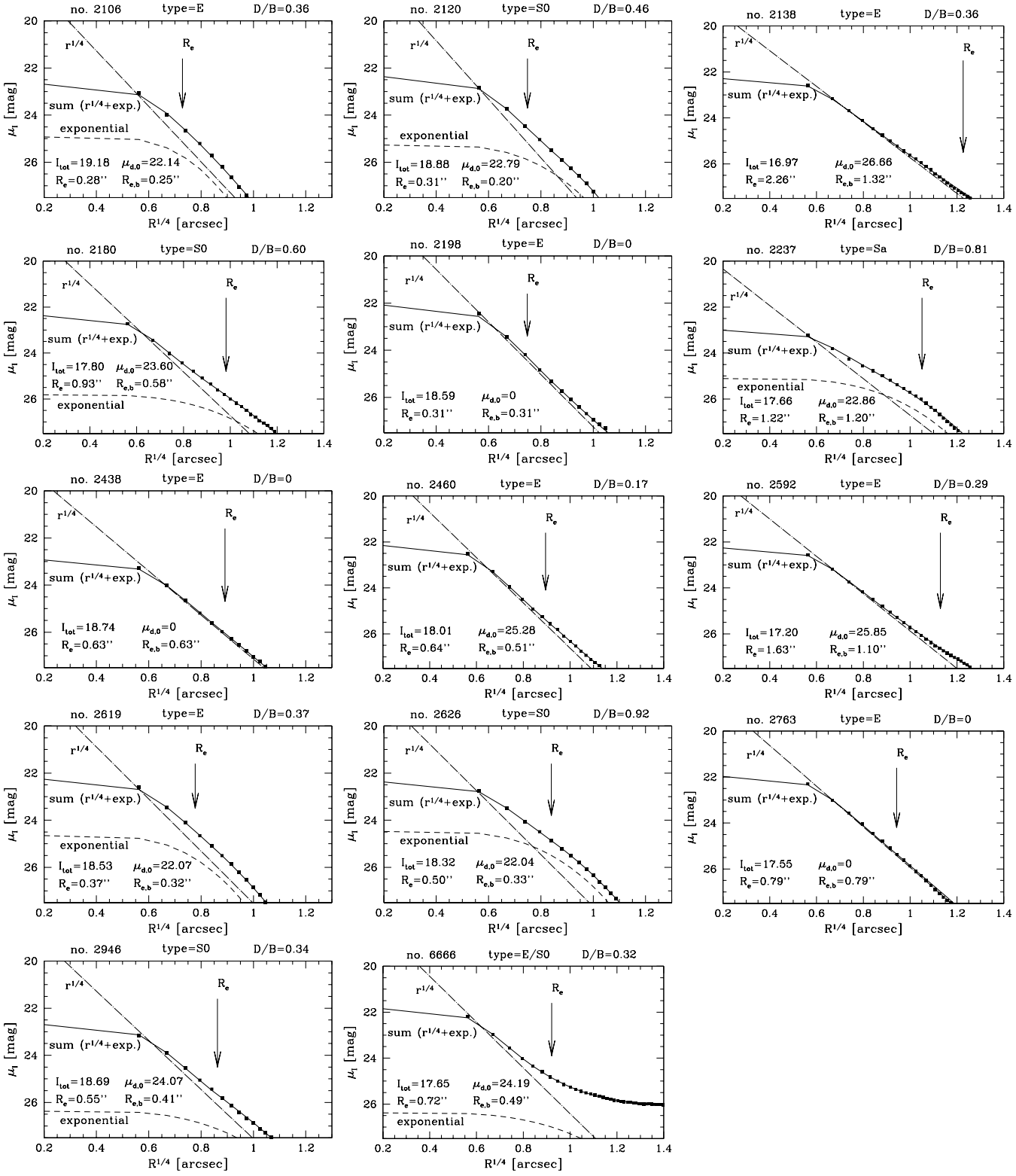

Figure A1. I_{814} Surface brightness profiles of galaxies residing within the *HST* image with available spectral information. The I_{814} surface brightness magnitude (extinction A_{F814W} corrected) is plotted against the radius $R^{1/4}$ (in arcsec). Filled squares show the observed profile, lines the different best models for the bulge (de Vaucouleurs law), disc (exponential law) component fit and for a combination of bulge and disc components (sum: $r^{1/4}$+exp. law). The arrow indicates the position of the effective radius R_{e}. Some structural parameters are given (see the text for details).

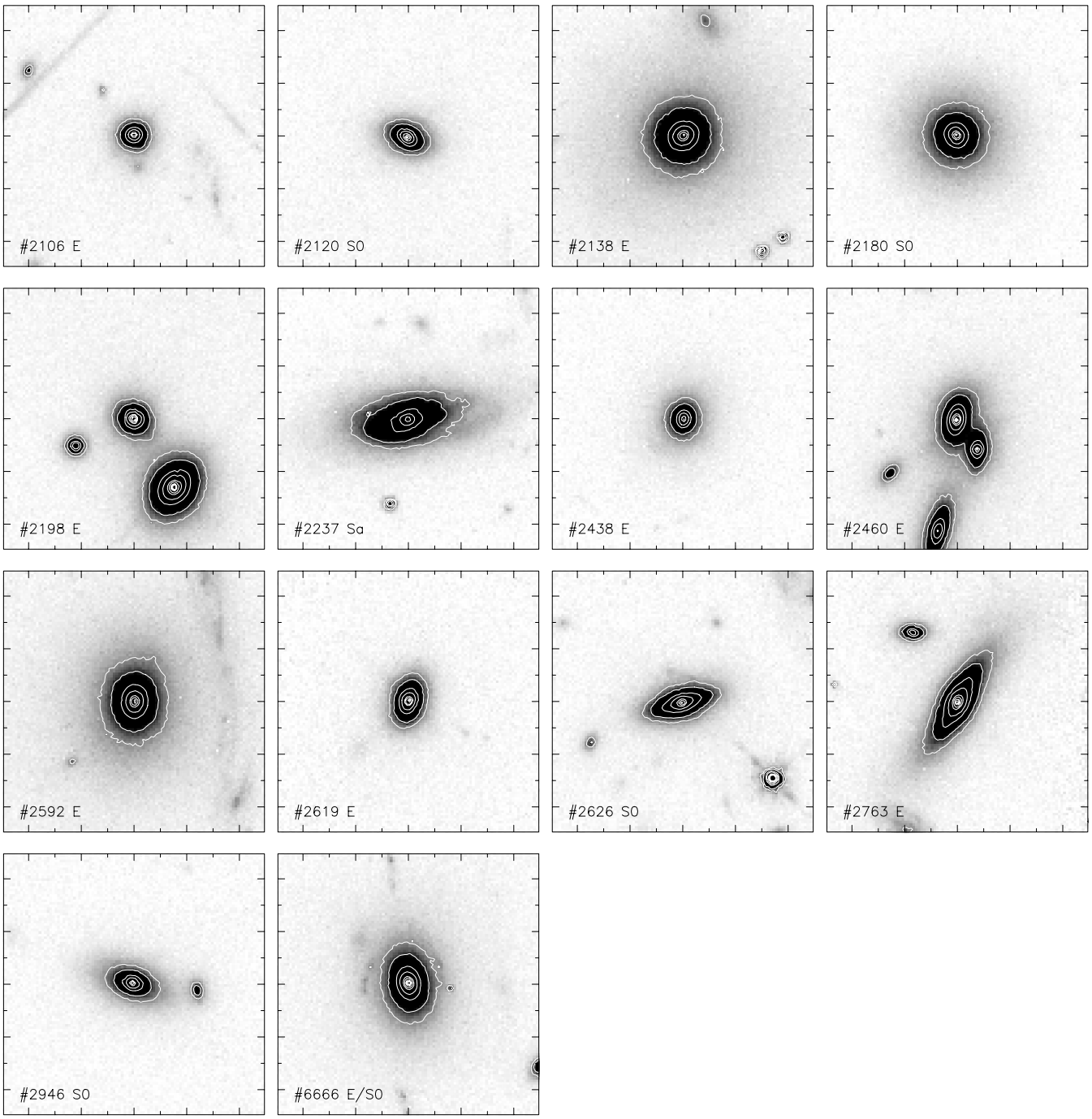

Figure A2. 10×10 arcsec^2 *HST*/WFPC2 images of 14 galaxies with available spectroscopic information which fall within the *HST*/*WFPC2* field of A 2390. The labels give the galaxy ID and the visual morphology as listed in Table 2. North is up and east is to the left. The colour coding ranges from white (sky background at $\sim$26.30 mag arcsec^{-2}) to black ($\leqslant$23.11 mag arcsec^{-2}). Isophotal contours are indicated between the range $24.50 \leqslant C_i \leqslant 21.94$ mag arcsec^{-2}, in increments of 0.5 mag.

Table A1. Note remarks on individual *HST* objects in Abell 2390.

ID	Morp	Comment
2120	S0	Signs of isophotal twists out to outer isophote
2138	E	Very extended low-surface brightness (LSB) environment
2198	E	Close to a bright neighbour
2237	Sa	[O III] 5007 and Hβ emission, asymmetric LSB extension
2460	E	Lensed?, very close to S0
2592	E	Next to giant arc
2763	E	Slight twisted low SB
2946	S0	Small companion
2933	Sbc	No member, no structural analysis, weird spiral structure, no interaction

Table B1. Properties of Abell 2390 cluster members.

ID	RA (J2000)	Dec. (J2000)	v (km s^{-1})	σ (km s^{-1})	S/N ratio	$I_{\rm tot}$ (mag)	M_r (mag)	$U_{\rm ap}$ (mag)	$B_{\rm ap}$ (mag)	$I_{\rm ap}$ (mag)
803	21:53:37.851	+17:38:26.50	67 851.4 ± 17	148.0 ± 15	24	18.47	−21.21	22.930 ± 0.045	22.346 ± 0.012	18.849 ± 0.002
869	21:53:46.482	+17:38:19.79	67 329.8 ± 13	106.9 ± 15	33	18.86	−20.82	23.414 ± 0.069	22.687 ± 0.014	19.364 ± 0.005
943	21:53:40.247	+17:37:59.77	69 571.0 ± 10	204.6 ± 08	40	16.69	−22.99	22.305 ± 0.026	21.588 ± 0.008	17.993 ± 0.002
1254	21:53:49.782	+17:39:14.32	68 452.1 ± 18	106.4 ± 18	23	19.03	−20.65	23.140 ± 0.053	22.714 ± 0.015	19.467 ± 0.003
1345	21:53:47.789	+17:39:25.65	70 862.4 ± 14	129.1 ± 12	30	18.65	−21.03	22.934 ± 0.046	22.456 ± 0.014	19.180 ± 0.003
1493	21:53:46.838	+17:39:49.11	68 239.0 ± 15	154.4 ± 16	28	18.60	−21.08	23.138 ± 0.054	22.490 ± 0.013	19.057 ± 0.002
1712	21:53:54.375	+17:40:06.60	68 509.8 ± 15	095.4 ± 17	29	19.13	−20.55	23.839 ± 0.104	23.184 ± 0.025	19.711 ± 0.003
1787	21:53:36.848	+17:40:34.89	68 215.8 ± 11	153.3 ± 14	37	18.37	−21.31	23.075 ± 0.054	22.296 ± 0.012	18.898 ± 0.003
1843	21:53:48.694	+17:40:24.96	69 626.6 ± 08	213.5 ± 07	55	17.21	−22.47	22.255 ± 0.027	21.485 ± 0.008	17.996 ± 0.003
1893	21:53:39.944	+17:40:37.38	72 079.8 ± 11	119.4 ± 13	40	18.58	−21.10	22.885 ± 0.041	22.229 ± 0.010	18.966 ± 0.003
1941	21:53:45.708	+17:40:43.92	68 936.3 ± 11	166.6 ± 14	37	18.32	−21.37	23.255 ± 0.064	22.394 ± 0.014	18.867 ± 0.002
1959	21:53:43.856	+17:40:49.44	69 561.5 ± 14	159.7 ± 16	29	18.62	−21.07	23.047 ± 0.047	22.385 ± 0.013	18.935 ± 0.002
1977	21:53:40.606	+17:40:50.81	69 353.9 ± 09	212.9 ± 11	48	18.40	−21.28	22.823 ± 0.042	22.249 ± 0.011	18.912 ± 0.003
1983	21:53:48.952	+17:40:46.37	68 611.0 ± 12	138.8 ± 14	35	18.53	−21.15	23.030 ± 0.050	22.352 ± 0.012	18.924 ± 0.002
2054	21:53:56.603	+17:40:38.70	67 758.9 ± 14	246.6 ± 10	34	17.43	−22.25	22.816 ± 0.044	22.019 ± 0.010	18.468 ± 0.002
2057	21:53:40.518	+17:41:03.88	70 311.6 ± 18	108.8 ± 18	24	19.21	−20.47	23.759 ± 0.100	22.947 ± 0.019	19.468 ± 0.004
2106	21:53:37.624	+17:41:09.49	70 303.6 ± 16	131.0 ± 16	26	18.66	−21.02	23.616 ± 0.081	22.933 ± 0.020	19.604 ± 0.005
2120	21:53:39.159	+17:41:08.84	68 348.1 ± 13	127.2 ± 15	34	18.69	−20.99	23.632 ± 0.081	22.840 ± 0.021	19.310 ± 0.004
2126	21:53:46.558	+17:40:56.81	68 688.5 ± 10	172.7 ± 10	40	18.01	−21.67	22.759 ± 0.041	22.074 ± 0.011	18.707 ± 0.002
2138	21:53:36.158	+17:41:12.92	73 905.5 ± 07	150.0 ± 08	54	17.45	−22.23	22.493 ± 0.030	21.737 ± 0.008	18.387 ± 0.002
2161	21:53:50.345	+17:40:58.65	65 805.4 ± 08	153.9 ± 09	55	17.28	−22.40	22.028 ± 0.021	21.373 ± 0.006	18.193 ± 0.002
2169	21:53:51.994	+17:40:58.94	69 318.7 ± 11	185.1 ± 10	39	16.99	−22.69	22.983 ± 0.052	22.288 ± 0.013	18.848 ± 0.002
2180	21:53:33.586	+17:41:27.44	68 429.8 ± 09	146.2 ± 10	49	18.07	−21.61	23.148 ± 0.056	22.262 ± 0.011	18.674 ± 0.002
2195	21:53:43.144	+17:41:19.67	71 527.1 ± 17	128.0 ± 18	25	19.20	−20.48	23.654 ± 0.085	22.899 ± 0.017	19.692 ± 0.003
2198	21:53:37.641	+17:41:24.93	70 010.9 ± 14	135.0 ± 15	31	18.84	−20.84	23.584 ± 0.081	22.589 ± 0.014	19.000 ± 0.002
2237	21:53:31.360	+17:41:34.36	73 707.2 ± 15	147.1 ± 12	29	17.83	−21.85	22.231 ± 0.025	21.693 ± 0.007	18.662 ± 0.002
2373	21:53:45.730	+17:41:32.35	68 244.0 ± 12	156.3 ± 11	34	17.58	−22.11	22.816 ± 0.039	21.913 ± 0.009	18.577 ± 0.002
2438	21:53:31.878	+17:41:59.61	71 101.3 ± 13	108.6 ± 15	30	19.04	−20.64	23.549 ± 0.077	22.787 ± 0.016	19.483 ± 0.003
2453	21:53:21.110	+17:42:06.57	69 447.8 ± 07	137.3 ± 08	60	17.27	−22.41	22.565 ± 0.047	21.845 ± 0.009	18.200 ± 0.002
2460	21:53:38.369	+17:41:47.78	69 519.3 ± 11	234.5 ± 10	40	17.78	−21.90	23.125 ± 0.054	22.194 ± 0.011	18.582 ± 0.002
2511	21:53:28.182	+17:42:12.63	69 317.2 ± 21	139.8 ± 18	21	19.07	−20.61	23.795 ± 0.098	22.965 ± 0.019	19.504 ± 0.003
2537	21:53:42.673	+17:41:53.94	67 004.5 ± 11	188.8 ± 13	35	18.03	−21.65	22.854 ± 0.043	22.182 ± 0.011	18.808 ± 0.002
2592	21:53:34.514	+17:41:57.74	68 966.4 ± 09	174.1 ± 11	45	17.47	−22.21	22.870 ± 0.044	21.919 ± 0.009	18.444 ± 0.002
2619	21:53:35.931	+17:42:13.22	69 424.2 ± 14	207.9 ± 14	30	18.74	−20.94	23.535 ± 0.076	22.606 ± 0.014	19.011 ± 0.002
2626	21:53:34.492	+17:42:14.28	67 821.9 ± 13	177.4 ± 12	32	18.47	−21.21	23.331 ± 0.063	22.371 ± 0.012	18.890 ± 0.002
2763	21:53:31.400	+17:42:28.91	65 665.2 ± 10	272.5 ± 12	51	17.64	−22.05	22.792 ± 0.042	21.889 ± 0.009	18.354 ± 0.002
2946	21:53:35.048	+17:42:49.44	72 296.1 ± 12	119.6 ± 15	34	18.81	−20.87	23.477 ± 0.070	22.834 ± 0.016	19.280 ± 0.003
3028	21:53:25.715	+17:43:40.70	70 038.0 ± 16	143.1 ± 11	27	18.44	−21.24	23.481 ± 0.083	22.607 ± 0.014	19.095 ± 0.002
3053	21:53:36.433	+17:44:13.33	68 419.5 ± 11	227.0 ± 13	39	17.94	−21.74	22.886 ± 0.044	22.004 ± 0.009	18.502 ± 0.002
3060	21:53:30.898	+17:44:45.62	69 644.6 ± 21	147.3 ± 16	21	18.58	−21.10	23.573 ± 0.085	22.724 ± 0.017	19.265 ± 0.003
3201	21:53:22.506	+17:44:10.77	67 835.1 ± 15	175.6 ± 17	29	19.13	−20.55	24.010 ± 0.167	23.171 ± 0.022	19.598 ± 0.003
3473	21:53:25.146	+17:44:16.95	66 780.5 ± 08	140.4 ± 10	49	18.06	−21.63	23.143 ± 0.067	22.236 ± 0.014	18.642 ± 0.002
3529	21:53:30.135	+17:43:57.75	71 026.3 ± 13	125.7 ± 10	32	18.15	−21.53	23.154 ± 0.060	22.336 ± 0.012	18.802 ± 0.002
3760	21:53:47.760	+17:42:45.52	72 378.9 ± 10	147.7 ± 12	39	17.92	−21.76	22.724 ± 0.038	21.968 ± 0.009	18.665 ± 0.003
3805	21:53:27.091	+17:43:36.42	69 601.5 ± 11	227.7 ± 07	41	17.42	−22.26	22.791 ± 0.044	21.870 ± 0.009	18.189 ± 0.002
3814	21:53:28.668	+17:42:52.37	68 365.3 ± 09	220.2 ± 10	49	17.19	−22.49	22.698 ± 0.045	21.872 ± 0.009	18.238 ± 0.002
3824	21:53:27.658	+17:45:06.43	66 326.5 ± 06	147.4 ± 08	65	18.13	−21.55	22.110 ± 0.025	21.679 ± 0.007	18.488 ± 0.002
6666	21:53:39.059	+17:42:59.13	67 163.3 ± 15	191.3 ± 13	28	17.68	−22.00	–	–	–

Table B2. Properties of non-cluster members.

ID	RA	Dec. (J2000)	v (km s^{-1})	σ (km s^{-1})	S/N ratio	$I_{\rm tot}$ (mag)	M_r (mag)	$U_{\rm ap}$ (mag)	$B_{\rm ap}$ (mag)	$I_{\rm ap}$ (mag)
1507	21:53:45.512	+17:39:57.40	98 182.2 ± 50	–	–	19.52	−20.16	23.778 ± 0.091	22.735 ± 0.015	19.645 ± 0.003
1639	21:53:57.073	+17:39:58.11	97 402.8 ± 50	–	–	19.46	−20.22	24.032 ± 0.121	22.976 ± 0.020	19.580 ± 0.003
2933	21:53:32.404	+17:42:48.76	119 347.6 ± 50	–	–	19.47	−20.21	23.688 ± 0.092	23.221 ± 0.024	19.979 ± 0.004
3038	21:53:27.845	+17:44:23.82	53 904.0 ± 08	211.0 ± 09	50	17.77	−21.91	22.197 ± 0.026	21.537 ± 0.006	18.249 ± 0.002

This paper has been typeset from a TEX/LATEX file prepared by the author.